



**HAL**  
open science

## A review of history parameters in PWR core analysis

Ea. Szames, D. Tomatis

► **To cite this version:**

Ea. Szames, D. Tomatis. A review of history parameters in PWR core analysis. *Annals of Nuclear Energy*, 2018, 10.1016/j.nucengdes.2019.03.012 . cea-02339996

**HAL Id: cea-02339996**

**<https://cea.hal.science/cea-02339996>**

Submitted on 22 Oct 2021

**HAL** is a multi-disciplinary open access archive for the deposit and dissemination of scientific research documents, whether they are published or not. The documents may come from teaching and research institutions in France or abroad, or from public or private research centers.

L'archive ouverte pluridisciplinaire **HAL**, est destinée au dépôt et à la diffusion de documents scientifiques de niveau recherche, publiés ou non, émanant des établissements d'enseignement et de recherche français ou étrangers, des laboratoires publics ou privés.



Distributed under a Creative Commons Attribution - NonCommercial 4.0 International License

# A review of history parameters in PWR core analysis

Esteban Szames and Daniele Tomatis\*

DEN, Service d'étude des réacteurs et de mathématiques appliquées,  
CEA, Université Paris-Saclay,  
F-91191 Gif-sur-Yvette, France

September 4, 2018

## Abstract

We present a review of the methodologies for history effect modelling with few-group cross sections for PWR fuel assemblies. Different depletion conditions with varying moderator density, fuel temperature and protracted control rod insertion are considered where the exposure history can show significant changes in the local isotopic inventory and in the neutron spectra. Cross sections are homogenized over a classical PWR-type  $\text{UO}_2$  fuel assembly provided by the Burn-up Credit Criticality Benchmark NEA-6227 and condensed in two energy groups by the lattice code APOLLO2.8. The methodologies are analyzed in view of their capability to improve the error in microscopic and macroscopic cross sections, and the associated multiplication factor and the spectral index in the infinite homogeneous medium.

**Keywords** — Cross section preparation, PWR, history effects, protracted control by mechanical shim

## Contents

|          |   |          |
|----------|---|----------|
| <b>1</b> | <b>Introduction</b>   | <b>2</b> |
| <b>2</b> | <b>Core calculations and few-group cross section models</b> | <b>2</b> |
| <b>3</b> | <b>History effects phenomena</b>                            | <b>3</b> |
| <b>4</b> | <b>History parameters</b>                                   | <b>4</b> |
| <b>5</b> | <b>Use cases for numerical tests</b>                        | <b>6</b> |
| <b>6</b> | <b>Implementation</b>                                       | <b>8</b> |

---

\*Corresponding author: [daniele.tomatis@cea.fr](mailto:daniele.tomatis@cea.fr)

|          |  |           |
|----------|--|-----------|
| <b>7</b> | <b>Results</b>   | <b>11</b> |
| 7.1      | Analysis of the microscopic cross sections . . . . .                   | 11        |
| 7.2      | Analysis of the macroscopic cross sections . . . . .                   | 17        |
| 7.2.1    | Investigation of the poor performances in $\mathcal{B}_{e2}$ . . . . . | 17        |
| 7.3      | Analysis of the infinite multiplication factor . . . . .               | 21        |
| <b>8</b> | <b>Conclusion</b>  | <b>24</b> |
| <b>A</b> | <b>APOLLO2.8 calculations</b>  | <b>28</b> |
| <b>B</b> | <b>Macroscopic cross sections error</b>                                | <b>28</b> |

# 1 Introduction

This work presents a review of the different techniques reported in literature to account for the history effects in core calculations for the water-moderated nuclear reactors, which represent nowadays the majority of the power units operating worldwide. In Section 2 the traditional methodologies of cross section preparation are discussed. Section 3 presents the history effects occurring during normal operation, where exposure history may imply significant changes in the local isotopic inventory and in the neutron spectra.

A first order Taylor expansion for several history parameters is presented in Section 4 as suggested by many reviewed articles. Use cases based on the OECD-NEA Burn-up Credit Criticality Benchmark, Phase-IIID [1] are discussed in Section 5 in order to test the methods whose implementation is detailed in Section 6. Results for the corrected microscopic and macroscopic cross sections and for the infinite multiplication factor are presented in Section 7. Finally, the conclusion follows in Section 8.

# 2 Core calculations and few-group cross section models

The use of nodal methods has allowed in the past decades the development of very efficient core simulators to carry out 3D full core calculations for design and safety studies [2]. Major advances in homogenization and equivalence theory, which started in the late 70s, have provided the standard two-step methodology for modern nuclear computer codes [3, 4].

In industrial applications, core calculations are usually performed on coarse meshes and the thermal-hydraulic feedback is ensured by a few-group cross section model through non-linear iterations. The typical size of the cells (often called nodes) of the spatial mesh is about half of the assembly pitch ( $\sim 10$  cm), whereas the most frequent energy discretization employs only two groups, with a cutoff energy at 0.625 eV. Generally, the core codes treat second order forms of the transport equations for neutrons, with  $SP_N$  approximations becoming quite popular nowadays [5]. Although its physical validity holds generally to asymptotic regimes, it always yields a diffusion solution at the order 1 (with the P1-diffusion coefficient of  $\lambda_{tr}/3$  where  $\lambda_{tr}$  is the transport mean free path).

A few-group cross section model provides the homogenized cross sections and possibly additional equivalence factors, like the assembly discontinuity factors. These are input data of the nodal balance equation resolved by a lower order transport operator on a coarse mesh in space. For the isotope  $i$  and the reaction  $r$ , this entails basically a projection on the region  $\mathcal{V}$ , and on the energy group  $g$  as:

$$\sigma_{\mathcal{V},i,r,g} = \frac{\int_g \int_{\mathcal{V}} (\sigma_{i,r} \phi)(\mathbf{V}, E) d\mathbf{V} dE}{\int_g \int_{\mathcal{V}} \phi(\mathbf{V}, E) d\mathbf{V} dE}, \quad (1)$$

with the space vector  $\mathbf{V} \in \mathcal{V} \subset \mathbb{R}^3$  and the neutron energy  $E$ . The neutron flux  $\phi$ , here considered as already integrated over the angle of flight of neutrons, comes from idealized 2D neutron transport calculations. These reproduce lattices of single or multiple fuel assemblies arranged in a periodic environment using the reflective boundary condition to prepare the data for all different types of fuel elements dictated by the core plan. About the reflector modelling, calculations in detailed environments of multiple assemblies (colorset calculations) are quite common.

Since the description of all existing nuclides present in the reactor core would prevent depletion calculations along exposure due to an unacceptable computational effort, only a limited amount is considered with the introduction of reduced depletion chains, characterizing further the cross section model. The number of the selected isotopes has increased in time as long as computational resources improved, showing now up to 150 specialized isotopes with more accurate fuel inventories. This is the current choice of modern core simulators, where all other minor isotopes are lumped together in a unique residual material (*res*), untracked by the code depletion solver. Macroscopic cross sections are then reconstructed as:

$$\Sigma = \Sigma_{res} + \sum_{j=1}^I \sigma_j N_j. \quad (2)$$

Among the  $I$  specialized isotopes, there are usually the most important fissile isotopes, fission products and burnable absorbers.

In order to represent operational and accidental conditions the homogenized data are functionalized by means of given “state parameters”, which are physical quantities showing high sensitivity on the neutron reactivity, being reactor-dependent as well. Common choices for water reactors are the thermo-dynamic properties of the coolant, as for instance the moderator temperature and/or its density, covering all regimes of heat transfer and thermal-hydraulics in the core, an average temperature in the fuel elements to reproduce the Doppler effect, the amount of  $^{135}\text{Xe}$  at equilibrium with the power level, the burnup in units of released thermal energy per unit of heavy metal or exposure time in Effective Full Power Days (EFPD), and the amount of diluted boron in water. The state parameters are determined by other models, i.e. thermal-hydraulics and isotopic depletion, employed in the core calculation to implement the multi-physics coupling [6].

The cross section data generated by lattice calculations are stored in external libraries to be accessed on demand by the core simulator. The wide range of possible reactor states are approximated as perturbed conditions with respect to a reference configuration, which is the most probable along fuel exposure at hot full power. So, “branch calculations” are derived for instantaneous changes at operation from a “nominal depletion history”, where the only varying state parameter is the burnup (or fuel exposure). The fuel inventory is calculated at different burnup steps using complete depletion chains, and critical neutron spectra achieved by a leakage model [7]. Self-shielding is here mandatory due to the resonant behavior of the constituting isotopes and to the possible spatial heterogeneity of the assembly design. Also, these assembly calculations often neglect any varying boron concentration in favor of an average value. Since the weighting neutron spectra depends on the exposure history, the lattice depletion conditions ought to be the most representative of the average core history for attaining accurate cross section reconstructions.

### 3 History effects phenomena

The few-group cross section data depends on the weighting neutron spectrum used at condensation and homogenization. In turn, this spectrum follows from the isotopic content resulting from previous depletion conditions. Hence, the inter-dependence of the spectrum and of the local concentrations at these given conditions defines a depletion history.

Whenever temporary deviations from the nominal conditions are noticed along the real exposure observed in the nodes of the core calculations, local spectra gets farer from those assumed a-priori at cross section preparation and the predicted homogenized cross sections may not be sufficiently accurate.

Exposure under different spectral conditions yields inevitably different nuclide contents and homogenizing spectra thus causing a “history effect”, or spectrum-induced error on the homogenized cross sections from lattice calculations.

This phenomenon is of particular importance in BWR reactor analysis due to the severe change of the void fraction along the core’s height and permanently controlled fuel assemblies in the bottom region. For instance, in the NEXUS package developed at Westinghouse three different depletion histories are usually considered [8] while some advanced BWR designs show up to four [9].

On the contrary, a single nominal history is usually chosen with PWRs, where branch calculations are motivated by relatively short insertion periods of control elements during power operation. History phenomena effects are usually considered as second order terms in PWR analysis, and this is certainly true for short deviations in time from nominal conditions.

Nonetheless, the need of load following capabilities has called for more controlled core patterns in PWRs, especially in France where the electrical power production is largely coming from nuclear power plants. In addition, it is possible to notice as a general trend in the design of new PWR units such as the EPR from AREVA [10] or the AP1000 from Westinghouse [11] enhanced control by gray banks permanently inserted or with prolonged insertion, with the goal of reducing the operational costs of the chemical shim. Moreover, innovative boron-free Small Modular Reactors envision control rods as a central feature for reactivity control at normal operation [12, 13, 14], motivating further the reason of this work.

The presence of control elements in the assemblies hardens the neutron spectrum because of increased absorption in the thermal range and decreased efficiency in the neutron slowing down rate. The strength of the control bank in the neutron absorption is indicated as gray or black. The first means only stainless steel in the rod cluster, while rods made of boron carbide ( $B_4C$ ) are also used for the second. Safety issues could arise such as an unexpected positive reactivity excess after the extraction of a bank inserted for a long period of time, because of a mistaken condensation by a softer spectrum and due to a higher amount of fissile material in the reactor with respect to the computed amount. Unfortunately, this kind of situations are rather frequent in real calculations, and they can be source of major error in a few extreme cases as shown by Tomatis et al. [15].

A similar process takes place with the enthalpy increase of the coolant along the fuel element’s channels resulting in different moderating conditions for neutrons. Although higher temperature promotes the scattering with hydrogen bound in water, the reduction of the moderator density decreases the neutron slowing-down rate. Spectrum hardening is expected towards the core outlet, and enhanced thermalization at inlet.

Another important phenomenon is the Doppler effect induced by the broadening of the resonances due to the thermal motion of nuclei with change of the fuel temperature. Different zones in the core, exposed to different power levels, can then undergo different spectral histories.

This requires the introduction of the history parameters, in addition to the customary instantaneous ones.

## 4 History parameters

In standard cross section preparation the isotopic changes along fuel exposure are represented by the burnup ( $Bu$ ), which can be considered as a first history parameter. The most probable physical conditions of exposure in the reactor define the nominal depletion history ( $\mathcal{B}_N$ ) and the state parameters are introduced to model a departure from such conditions.

Provided linear independence of all the parameters in the model, the general functionalization of the cross section is  $\sigma(Bu, \boldsymbol{\nu}, \boldsymbol{\theta})$ , where  $\boldsymbol{\nu} = (\nu_1, \dots, \nu_d)$  represents  $d$  instantaneous state parameters and  $\boldsymbol{\theta} = (\theta_1, \dots, \theta_h)$  features the set of  $h$  history parameters. The dependence on the first parameters is reproduced by branch calculations, while new depletion histories are used for the second ones. These last histories are called “off-nominal” in this work. A Cartesian grid is then constructed with all these calculation points provided that branch calculations are performed on all off-nominal calculations.

Of course, the selection of the supporting depletion calculations is driven by feasibility reasons according to the available computational resources. For instance, the size of the data libraries for core calculations is estimated in the order of several gigabytes, and even if computing a lattice calculation point is in the order of a few tenths of seconds, the library production time may become promptly prohibitive for the industrial work-frame. In the previous generation of core calculations few particularized isotopes ( $I \ll 10$ ) were used and history parameters were a needful requirement for realistic simulations. Denser depletion chains in core calculations have mitigated the history effects, moving the attention on the pin power distributions. Indeed non-conservative errors in the power form factors are reported by Martin et al. [6] and the use of history parameters was proposed by Dall’Osso et al. [16] to reduce them.

In an early work by Mosteller the moderator history was used for computing empirical corrective terms stored in look-up tables [17]. It is defined as a burnup-averaged quantity of the instantaneous moderator density  $\delta$ :

$$\text{MH} = \frac{1}{Bu} \int_0^{Bu} \delta(Bu') dBu'. \quad (3)$$

Later, in the code POLCA [18], cross sections calculated at hot full power (HFP) condition were corrected, with additive terms presenting a quadratic dependence with the MH. Nowadays, many industrial code simulators take into account history parameters, like SIMULATE-4 [19] or ARCADIA-BWR [6]. However, when several others history parameters are considered, a large number of additional depletion histories are required. This occurs with the code NECP [20] that accounts for the control rod and fuel temperature history for a total of 30 additional depletion calculations.

According to the available literature, a single history parameter was considered in PWR modelling. A common assumption asserts that changes in the cross sections induced by spectral variations can be considered as independent of its causing phenomenon [21]. The spectral history SH [22, 23] is defined as:

$$\text{SH} = \frac{1}{Bu} \int_0^{Bu} \frac{\text{SI}(Bu')}{\text{SI}_N(Bu')} dBu', \quad (4)$$

with the ratio between the actual spectral index (SI) and the one from the nominal calculation here indicated by the subscript  $N$ . The spectral index in the two-group model is the ratio of the fast flux  $\phi_1$  over the thermal flux  $\phi_2$  (cutoff energy at 0.625 eV):

$$\text{SI} = \phi_1 / \phi_2. \quad (5)$$

Although other definitions of the SI are noticed in literature [24, 25], they are not considered in this work in virtue of the simpler and standard definition above. For example, the code NEREUS [23] is reported to add a quadratic correction of the kind  $\sum_{i=0}^2 a_i(Bu)(\text{SH} - 1)^i$  to the macroscopic cross sections.

Despite the spectral index is here considered as an instantaneous parameter, the code PHOENIX/ANC used the SI evaluated at HFP and hot zero power (HZP) for correcting microscopic cross sections with a second order polynomial, whose coefficients came by ordinary least square regression. This correction was applied only to the fission and to the absorption thermal cross sections of  $^{235}\text{U}$  and  $^{239}\text{Pu}$  [26]. The model was later enhanced to correct also the fast group data [27], as reported in the Westinghouses code package NEXUS dedicated to LWR simulation [28].

An interesting study by Bilodid and Mittag [29] considers relative differences in the concentration of the  $^{239}\text{Pu}$ , here simply noted with the chemical symbol and the mass number, as a reliable indicator of the spectral history in the fuel. Changes in the homogenized cross sections affected by the history were found to be proportional to the square of  $^{239}\text{Pu}$  so a new history parameter was proposed with the following linearization [30]:

$$\text{P} = \sqrt{^{239}\text{Pu}}. \quad (6)$$

In the same work, it is explicitly stated as underlying hypothesis that correlations in the change of the isotopic content causing the history effect can be modeled with a unique history parameter. This method was implemented in the code DYN3D [31].

The SCIENCE code package by Framatome uses the ratio between the concentrations of all plutonium isotopes (Pu) and  $^{238}\text{U}$  to recover the history [32], i.e.

$$\text{PU} = \text{Pu}/^{238}\text{U}. \quad (7)$$

A new irradiation history with a different moderator density provides the additional off-nominal calculation for the parameterization. This interesting feature is retained in this work for the implementation of the different methodologies under study.

Several authors suggest a unique linear correction term [21, 17, 29, 33] for the history effect. In general, this can be formalized through first order Taylor expansions around the history parameter evaluated on the nominal depletion history, i.e.  $\sigma_N = \sigma(Bu, \boldsymbol{\nu}, \theta_N(Bu))$ . For every isotope, reaction, energy group and homogenization region it is:

$$\sigma(Bu, \boldsymbol{\nu}, \theta) \simeq \tilde{\sigma} = \sigma_N \left[ 1 + \frac{\theta_N}{\sigma_N} \frac{\partial \sigma}{\partial \theta} \Big|_{\theta=\theta_N} \left( \frac{\theta}{\theta_N} - 1 \right) \right]. \quad (8)$$

The history parameter  $\theta$  results from the actual node's state in the core calculation, while the value of  $\theta_N$  from the nominal depletion history must also be determined online within the core calculations. The derivative is approximated by finite differences requiring the additional "off-nominal" calculations at different depletion conditions. Although Equation 8 holds for any  $\boldsymbol{\nu}$ , the derivative term is assumed as weakly dependent on  $\boldsymbol{\nu}$  itself, so it is here evaluated at a given  $\hat{\boldsymbol{\nu}}$  as:

$$\frac{\partial \sigma}{\partial \theta} \Big|_{\theta=\theta_N} \simeq \frac{\partial \sigma}{\partial \theta} \Big|_{\theta=\theta_N, \boldsymbol{\nu}=\hat{\boldsymbol{\nu}}} \simeq \frac{\sigma_{off}(Bu, \hat{\boldsymbol{\nu}}, \theta_{off}(Bu)) - \sigma_N(Bu, \hat{\boldsymbol{\nu}}, \theta_N(Bu))}{\theta_{off} - \theta_N}. \quad (9)$$

This allows a reduction in the number of lattice calculations and also in the storage requirements. Considering  $\hat{\boldsymbol{\nu}}$  at the nominal state permits the evaluation at the most probable conditions of operations but requires an additional branch calculation on the supporting off-nominal history. This can be avoided by evaluating the derivative at the off-nominal condition. Of course, the same  $\hat{\boldsymbol{\nu}}$  is used in Equation 9 for the cross sections in order to capture only the target history effect. Lastly,  $\sigma_N$  is customarily reconstructed in the core calculation by interpolation on  $\boldsymbol{\nu}$  and  $Bu$ .

## 5 Use cases for numerical tests

A suite of use cases characterized by different depletion conditions are used to compare the accuracy of the techniques reported in Section 4. These cases are based on the OECD-NEA Burn-up Credit Criticality Benchmark (Phase-IIID), which studies the impact of control rod insertion on the fuel compositions and on the neutron reactivity [1]. Indeed, they allow to reproduce the behavior of the core's node delivering the actual  $\theta$  values for Equation 8 and the isotopes concentrations for Equation 2.

In Figure 1, the fuel assembly of  $17 \times 17$   $\text{UO}_2$  fuel rods with 4% enrichment w/o  $^{235}\text{U}$  and with 25 guide tubes is presented. As material and geometrical specifications are fully available in the benchmark report [1], we only recall here the most important information. A constant boron concentration of 456 ppm diluted in the moderator is imposed in all calculations.

Reflective boundary conditions are applied and spatial homogenization of nuclear data are performed over the whole assembly. Two-group homogenized cross sections are analyzed to comply with the industry standards. The target exposure of 45 GWd/t represents a plausible utilization option in a loading scheme with three batches per cycle. The lattice calculations are performed with APOLLO2.8, see Appendix A for the calculation options.

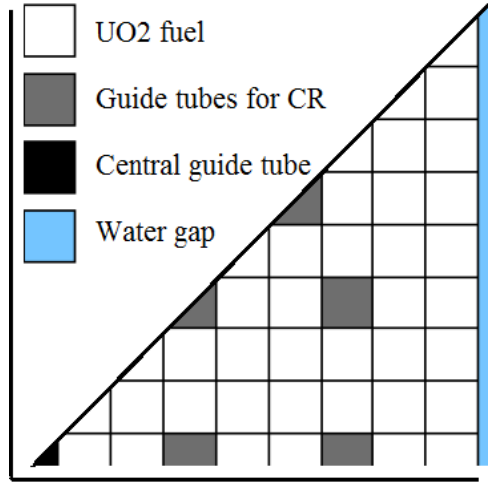


Figure 1: Layout of 1/4  $\text{UO}_2$  fuel element.

The irradiation histories calculated by the lattice code are denoted by the character  $\mathcal{B}$  in Table 1, with the subscripts indicating the different depletion conditions. These histories are reproduced by the curves  $(Bu, \iota_{\mathcal{B}}(Bu), \theta_{\mathcal{B}}(Bu))$  in the parameter space generated by  $Bu \otimes \iota \otimes \theta$ .

Table 1: Depletion histories considered to reproduce the history effects and to test the methodologies proposed in the literature. The insertion period of the control rods (CR-IP) is given in burnup units.  $T_f$  is the average fuel temperature in the pellets and  $\delta_M$  is the density of the cooling water.

|                    | Description                     | $T_f$<br>[°C] | $\delta_M$<br>[g/cm <sup>3</sup> ] | CR-IP<br>[GWd/t] |
|--------------------|---------------------------------|---------------|------------------------------------|------------------|
| $\mathcal{B}_N$    | Nominal condition               | 600           | 0.72                               | Out              |
| $\mathcal{B}_I$    | Inlet condition                 | 600           | 0.75                               | Out              |
| $\mathcal{B}_O$    | Outlet condition                | 600           | 0.66                               | Out              |
| $\mathcal{B}_f$    | High fuel temperature           | 1200          | 0.72                               | Out              |
| $\mathcal{B}_{c1}$ | CR in the 1 <sup>st</sup> cycle | 600           | 0.72                               | In [0,15]        |
| $\mathcal{B}_{c2}$ | CR in the 2 <sup>nd</sup> cycle | 600           | 0.72                               | In [15,30]       |

$\mathcal{B}_N$ ,  $\mathcal{B}_I$  and  $\mathcal{B}_O$  are respectively the irradiation histories at nominal, inlet and outlet conditions. Branch calculations are executed only on these depletion histories for computing the derivatives and to implement the methodologies.  $\mathcal{B}_f$  presents a case with high temperature in the fuel, which is noticed by Baturin [24] as a challenging condition for spectral history modelling.

Gray control rods made of stainless steel AISI316L with a density of 7.8481 g/cm<sup>3</sup> and suited for reactor control by prolonged insertion, are used in the first cycle for  $\mathcal{B}_{c1}$  and in the second cycle for  $\mathcal{B}_{c2}$ . Their specification is presented in table 2. They are characterized by an inner radius of 0.18840 cm and outer radius of 0.43130 cm.

In our calculations, the power level is not modified when the assembly is depleted with the control rods inserted. These are the only cases where the depletion conditions change along exposure. All off-nominal cases provide reference cross section values at distinct depletion conditions for benchmarking the physical accuracy.

Table 2: Material composition of the AISI316L control rods. The superscript “nat” denotes chemical elements with the natural isotopic abundances, see [34].

| Isotope           | Concentration [1/barn/cm] |
|-------------------|---------------------------|
| <sup>nat</sup> Fe | $5.5366 \times E^{-02}$   |
| <sup>nat</sup> Cr | $1.5452 \times E^{-02}$   |
| <sup>nat</sup> Ni | $9.6629 \times E^{-03}$   |
| <sup>nat</sup> Mo | $1.2317 \times E^{-03}$   |
| <sup>55</sup> Mn  | $1.7206 \times E^{-03}$   |
| <sup>nat</sup> Si | $1.6827 \times E^{-03}$   |
| <sup>nat</sup> C  | $3.1505 \times E^{-04}$   |

The set of specialized isotopes is :

$$\mathcal{I}_I = \{^{109}\text{Ag}, ^{243}\text{Am}, ^{153}\text{Eu}, ^{155}\text{Gd}, ^{95}\text{Mo}, ^{143}\text{Nd}, ^{145}\text{Nd}, ^{237}\text{Np}, ^{238}\text{Pu}, ^{239}\text{Pu}, ^{240}\text{Pu}, \\ ^{241}\text{Pu}, ^{242}\text{Pu}, ^{103}\text{Rh}, ^{101}\text{Ru}, ^{147}\text{Sm}, ^{149}\text{Sm}, ^{150}\text{Sm}, ^{151}\text{Sm}, ^{152}\text{Sm}, ^{99}\text{Tc}, ^{234}\text{U}, \\ ^{235}\text{U}, ^{236}\text{U}, ^{238}\text{U}, ^{133}\text{Cs}, ^{135}\text{Xe}, ^{135}\text{I}\}. \quad (10)$$

The remaining isotopes are lumped together in a residual macroscopic cross section ( $\Sigma_{res}$ ), with a total number of isotopes  $I = 28 + 1$ , see Equation 2.

An overview of the departure of the history parameters from the nominal case is presented in Figure 2. The plotted relative values allow to easily determine the term  $(\theta/\theta_N - 1)$  of Equation 8 and to show the variation among the history parameters for the different depletion histories.

The spectrum hardening, noticed at the outlet condition with a 15% increment of the SI, promotes the production of <sup>239</sup>Pu by an increasing capture rate of <sup>238</sup>U due to epithermal resonances. All cases show  $\theta_B > \theta_N$  but the inlet  $\mathcal{B}_I$ , which is the only depletion curve that exhibits a decrease in the Pu concentration caused by a softer spectrum.

The monotone behavior of the SI within the fuel cycles results from the hardening of the neutron spectrum with exposure since the fissile material in the fuel is depleted at a constant power level. When the movement of the control rod changes the configuration of the assembly, the SI shows discontinuity because of the high reactivity worth of the isotopes in the control rods. Instead the SH always responds in a continuous way due to its integral definition. After the control rod is withdrawn, the history parameters tend towards their nominal values.

## 6 Implementation

As defined in Equation 8, off-nominal calculations are needed to use a new parameterization on  $\theta$  and for the evaluation of the derivative in Equation 9. The same Equation 8 is specifically introduced in this work to have a common basis to compare the performances of the different methodologies under reviewing and to offer a unique implementation. The possibilities to implement the methods considered in this work are presented in Table 3 and tested with the use cases defined in Table 1.

Since the most of the cases show history effects similar to those caused by spectrum hardening at the core outlet, we choose  $\mathcal{B}_O$  as the off-nominal depletion history to implement the different methodologies from Section 4. All the combinations of  $\theta_{off}$  and  $\tilde{\ell}$  are considered only with the parameter P. As well, in the PU method the sum is performed over all available plutonium isotopes from  $\mathcal{I}$ , see Equation 10. The methods P1, P2, P3, P4 are here indicated by P\*, and when also considering PU they are referred to as “the Pu methods”, while those based on SI and SH are called “the spectral methods”.

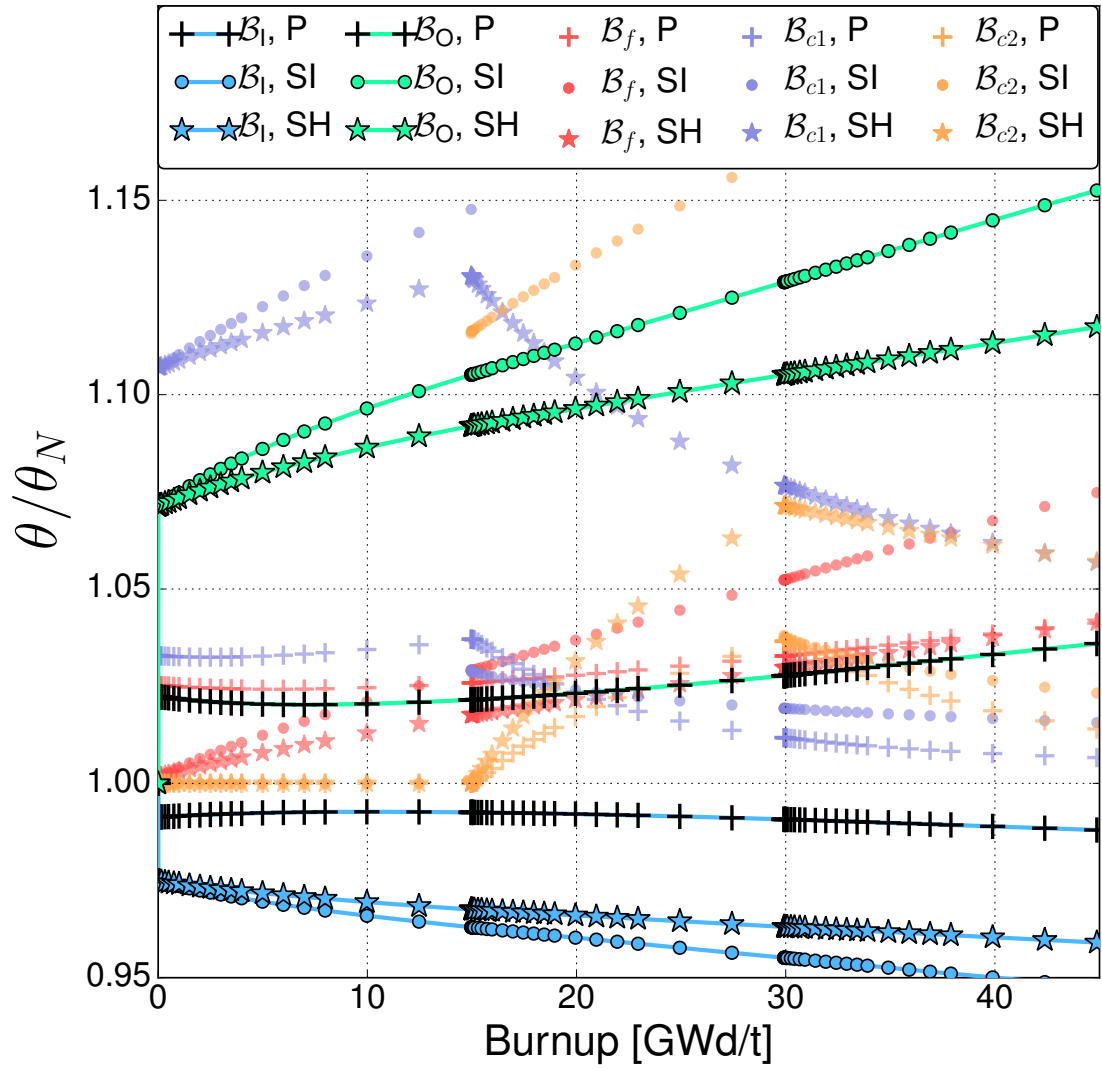


Figure 2: Ratio of the history parameters P, SH, SI for the different use cases over the nominal case.

Table 3: Description of the history effect parameterization; Numbers in the second column refer to the equations used to define the given history parameter, whereas the depletion histories whose parameters belong to are indicated in the others.

| Method | History parameter ( $\theta$ ) | Off-nominal history ( $\theta_{off}$ ) | Instantaneous parameter ( $\hat{i}$ ) |
|--------|--------------------------------|--|---------------------------------------|
| P1     | (6)                            | $\mathcal{B}_I$                        | $\mathcal{B}_I$                       |
| P2     |                                |  | $\mathcal{B}_N$                       |
| P3     |                                | $\mathcal{B}_O$                        | $\mathcal{B}_O$                       |
| P4     |                                |  | $\mathcal{B}_N$                       |
| PU     | $\mathcal{B}_O$                |  | $\mathcal{B}_O$                       |
| SI     |                                |  |                                       |
| SH     |                                |  |                                       |
| MH     | (3)                            |  |                                       |

When performing statistical analysis only points where the history effect has taken place are considered so the first cycle of  $\mathcal{B}_{c2}$  is excluded, and points with 0 exposure for all the cases. For uncorrected, P1, P2 and P4 all the use cases are considered. For P3, PU, SH, SI all cases except  $\mathcal{B}_O$  are considered. For MH only  $\mathcal{B}_I$  is considered.

Figure 3 illustrates briefly how the corrections are computed. The coefficients  $S = (\theta_N/\sigma_N)(\Delta\sigma/\Delta\theta)$  are determined by  $\sigma_N$  and  $\sigma_{off}$  evaluated at  $\hat{i}$  by means of branch calculations for different values of the fuel assembly burnup. They are then stored on data libraries for subsequent core calculations, where the cross section  $\sigma_N$  corrected by  $S$  will provide  $\tilde{\sigma}$ , i.e. an approximation of the target value  $\sigma$  (in green). These coefficients become part of the process of the cross section preparation and they must be stored in the few-group cross section library.

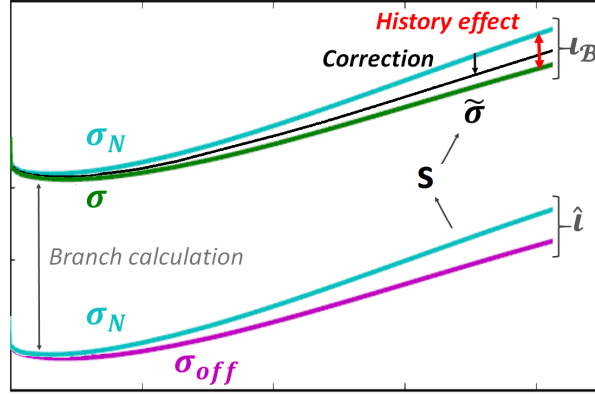


Figure 3: Scheme of the history parameterization.

The history coefficients of a few important isotopes are presented in Figure 4 as an example. The importance of an isotope is here estimated simply as the fraction of macroscopic cross sections as  $(C_i\sigma_{i,r,g})/\Sigma_{r,g}$  where  $C_i$  is the nuclide concentration of the isotope  $i$ . The isotopes shown in Figure 4 are those that demonstrate higher importance for the most of the whole exposure length. Although other definitions focusing on the isotope importance for the neutron reactivity are available from perturbation theory, this choice allows for fast classifications when analyzing the results. The absolute values of the coefficients

start at zero, since no history effect has taken place yet, to then smoothly increase with the burnup. In general if  $\theta_{off} > \theta_N$ , negative values can be seen as a harder spectrum lowers the overall chance of neutron capture in the thermal energy range, i.e.  $\sigma_O < \sigma_N$  and contrarily  $\sigma_I > \sigma_N$ . If  $\theta_{off} < \theta_N$ , like with the method MH, the coefficients are usually positive. Neutron up-scattering increases with a harder spectrum whereas down-scattering decreases.

The weak dependence of the coefficients on  $\hat{t}$  is shown in Figure 5 for the coefficient of  $\sigma_{a,1}$  of the isotope  $^{240}\text{Pu}$ , in fact negligible differences can be observed between P1 and P2 and between P3 and P4. This allows to avoid additional branch calculations on the off-nominal depletion calculation (here  $\mathcal{B}_I$  or  $\mathcal{B}_O$ ) to homogenize new cross sections at the nominal condition  $\hat{t}_N$ . The observations about the  $^{240}\text{Pu}$  are a general trend for all other isotopes.

On the other hand, a significant difference of up to 25% can be noticed by changing  $\theta_{off}$  from inlet to outlet, like from P1 to P3 for instance. This indicates possible non linearity and relevance of the higher order terms in the Taylor expansion, here disregarded to comply with the methods from the literature. Smaller absolute values for the SI and for the SH coefficients are observed with respect to the Pu methods.

## 7 Results

The performance of the methods to predict accurate microscopic and macroscopic cross sections ( $\sigma$  and  $\Sigma$ ), still homogenized in the fuel assembly quarter and condensed in the two group energy mesh, is studied in this section. The multiplication factor and the fundamental flux calculated by the associated eigenvalue problem in the infinite homogeneous medium are also analyzed.

### 7.1 Analysis of the microscopic cross sections

The relative error of the microscopic cross sections for each isotope, reaction and energy group is defined as:

$$\epsilon_{\sigma, \mathcal{B}, \theta}(Bu) = \tilde{\sigma} / \sigma_{\mathcal{B}} - 1. \quad (11)$$

$\tilde{\sigma}$  comes from Equation 8 while  $\sigma_{\mathcal{B}}$  is calculated on the depletion history  $\mathcal{B}$ . Although both cross sections are evaluated over the curve  $(Bu, \iota_{\mathcal{B}}(Bu), \theta_{\mathcal{B}}(Bu))$  the isotopic inventories of the corresponding calculations reproducing them by homogenization differ. Branch calculations are performed at  $\iota_{\mathcal{B}}(Bu)$  thus avoiding the need of any interpolation to determine  $\sigma_N$  and the introduction of other source of error. Relative errors permit to account for every  $\sigma$  regardless of the variations in their absolute values.

Illustrative examples of the history effects are presented in Figure 6 for the thermal fission production cross section of  $^{235}\text{U}$ ,  $\nu\sigma_{f,2}$ . For instance in  $\mathcal{B}_{c1}$ , a maximum error of 8 barn, about 1.35%, is achieved at the end of the first cycle for the uncorrected cross section ( $\sigma_N$  in light blue). This error is often reduced when considering the corrections of the history parameters, that is approaching the green curves of the reference target values. After the withdrawal of the control rod at 15 GWd/t in  $\mathcal{B}_{c1}$  and at 30 GWd/t in  $\mathcal{B}_{c2}$ , the SI exhibits a prompt response underestimating the intended correction, while the SH shows a delayed response typical of its integral character. The Pu method provides better correction here with this fissile isotope.

A simple arithmetic average of the absolute error is proposed in the following to assess a global overview of the behavior of the error:

$$\varepsilon_{\mathcal{B}, \theta}(Bu) = \frac{\sum_{i=1}^I \sum_r \sum_g |\epsilon_{\sigma_{i,r,g}}|}{M}, \quad (12)$$

where  $I$  is inferred from Equation 10, and the sum on the reactions and energy groups is taken on the elements of the set  $\{\nu\sigma_{f,1}, \nu\sigma_{f,2}, \sigma_{a,1}, \sigma_{a,2}, \sigma_{1 \rightarrow 2}, \sigma_{2 \rightarrow 1}\}$ .  $M$  is the total number of terms in the sum. These averages provide a global trend, without any quantification of the error on the neutron reactivity, treated further on. They are available for all cases  $\mathcal{B}$  and history parameters  $\theta$ . The in-scattering cross sections are disregarded in this study, because they can be removed from the neutron balance equation. Figures 7 show the averages  $\varepsilon$  in the two cases  $\mathcal{B}_{c1}$  and  $\mathcal{B}_{c2}$ .

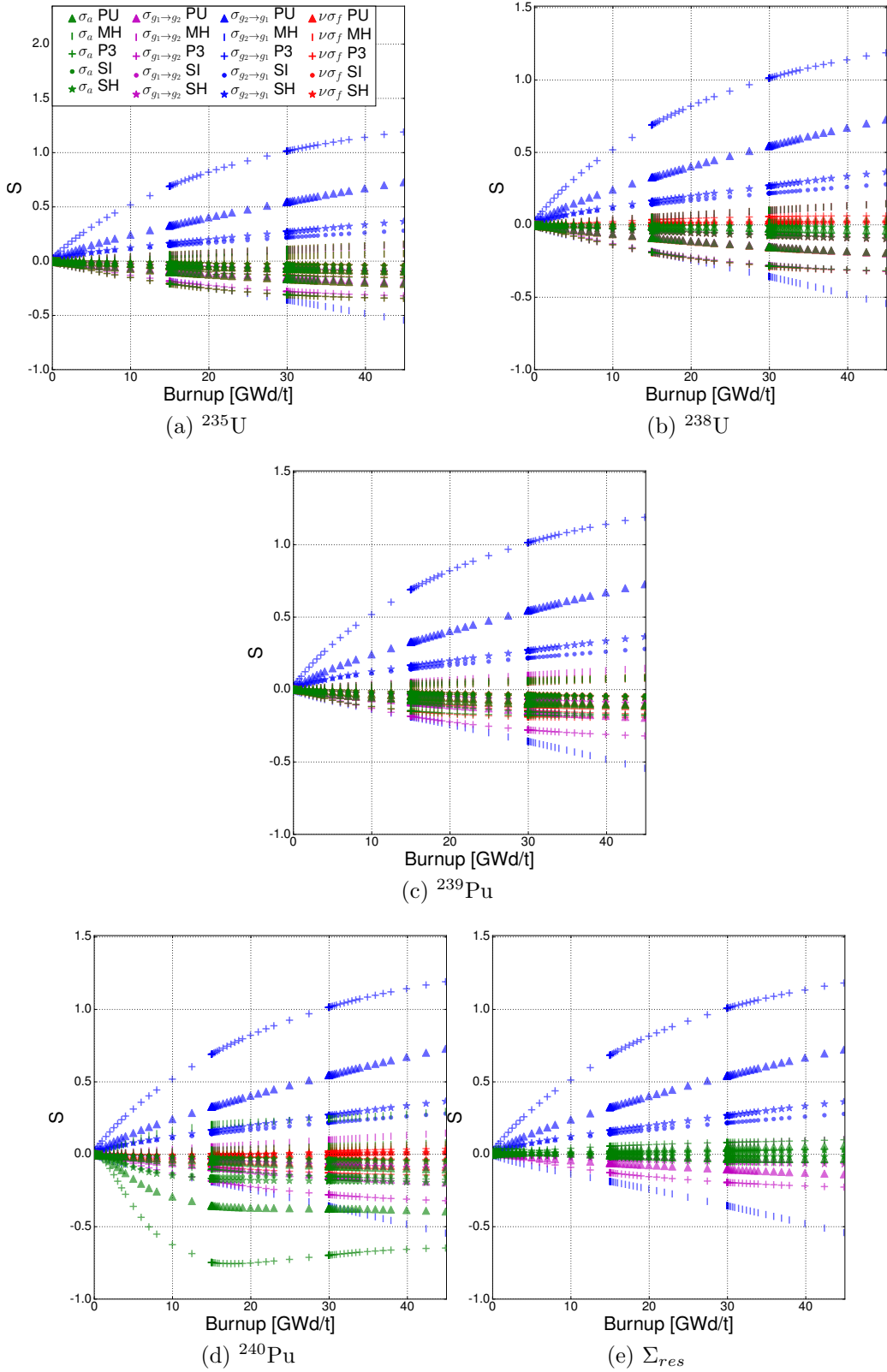


Figure 4: History coefficients of the most important isotopes.  $\sigma_a$  and  $\nu\sigma_f$  identify the values of both the fast and the thermal groups. The legend in the plot of  $^{235}\text{U}$  is common to the other figures.

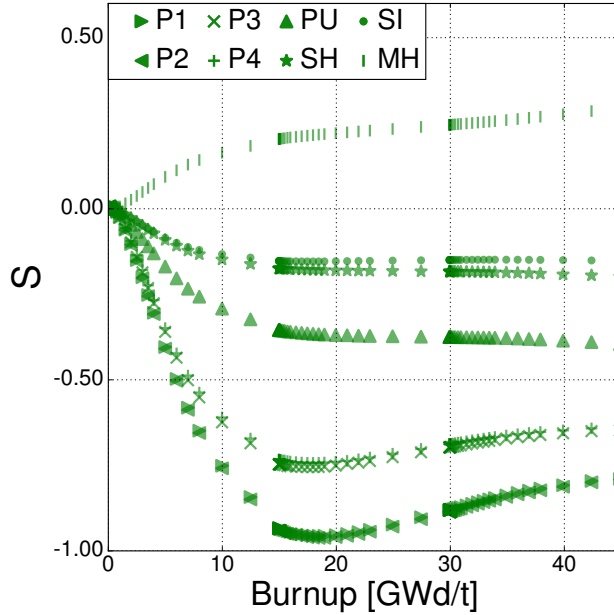


Figure 5: History coefficients of  $\sigma_{a,1}$  of  $^{240}\text{Pu}$  for the history parameters.

The uncorrected error shows a monotone behavior in the different cycles, with a negative trend after rod withdrawal. Maximum values around 1% are detected at the end of the insertion periods. General improvement is observed with the history parameters but for the SI, which overshoots its correction. As already mentioned above, the presence of strong neutron absorbers in the control rods has a considerable influence on the SI, and consequently also on the difference  $(\text{SI}/\text{SI}_N - 1)$  in Equation 8. In the first cycle of  $\mathcal{B}_{c1}$ , the module of its history coefficient varies smoothly with the burnup, see Figure 4, and so it does accordingly the average error on all the microscopic cross sections. After the control rods are withdrawn,  $\text{SI}/\text{SI}_N$  gets closer to 1 since the isotopic contents, produced under different depletion conditions, have a negligible impact on the neutron spectrum in the assembly and  $\varepsilon_{\mathcal{B}_{c1},\text{SI}}$  follows the profile of  $\varepsilon_{\mathcal{B}_{c1},N}$ . At the beginning of the second cycle in  $\mathcal{B}_{c2}$  the severe jump of the SI, together with non-zero history coefficients, leads to un-physical  $\tilde{\sigma}$ , even if no history effect has occurred yet.  $\mathcal{B}_{c2}$  seems slightly more challenging than  $\mathcal{B}_{c1}$  for the higher errors noticed. Besides, hidden compensation effects could be quite relevant by considering also the greater coefficients  $S$  and ratios  $\theta/\theta_N$  computed in the second cycle range. The method PU shows the best results by reducing the error below 0.1%, outperforming the other P\* methods.

Burnup-averaged errors offer quick comparisons to compare the performances of the methods in the use cases. They are defined hereafter within the generic interval  $(Bu_1, Bu_2)$  as:

$$\bar{\varepsilon}_{\mathcal{B},\theta} = \frac{1}{\Delta Bu} \int_{Bu_1}^{Bu_2} |\varepsilon_{\mathcal{B},\theta}(Bu)| dBu', \quad (13)$$

and presented in Figure 8 on the complete exposure interval  $([0,45] \text{ GWd/t})$  for  $\mathcal{B}_I$ ,  $\mathcal{B}_O$ ,  $\mathcal{B}_f$ , and separated per cycle for the other cases.

A reduction of one order of magnitude in the error is observed with all methods when testing against  $\mathcal{B}_I$  and  $\mathcal{B}_O$ . This fact is expected indeed, because these cases are used as off-nominal calculations to compute the history coefficients. Of course, when a case is used for the implementation of the correction method, then it is automatically neglected for the tests.

Since inlet conditions are closer to  $\mathcal{B}_N$ , the uncorrected average error is smaller. No significant change with different off-nominal calculations or history parameters can be seen for both  $\mathcal{B}_I$  and  $\mathcal{B}_O$ . The best

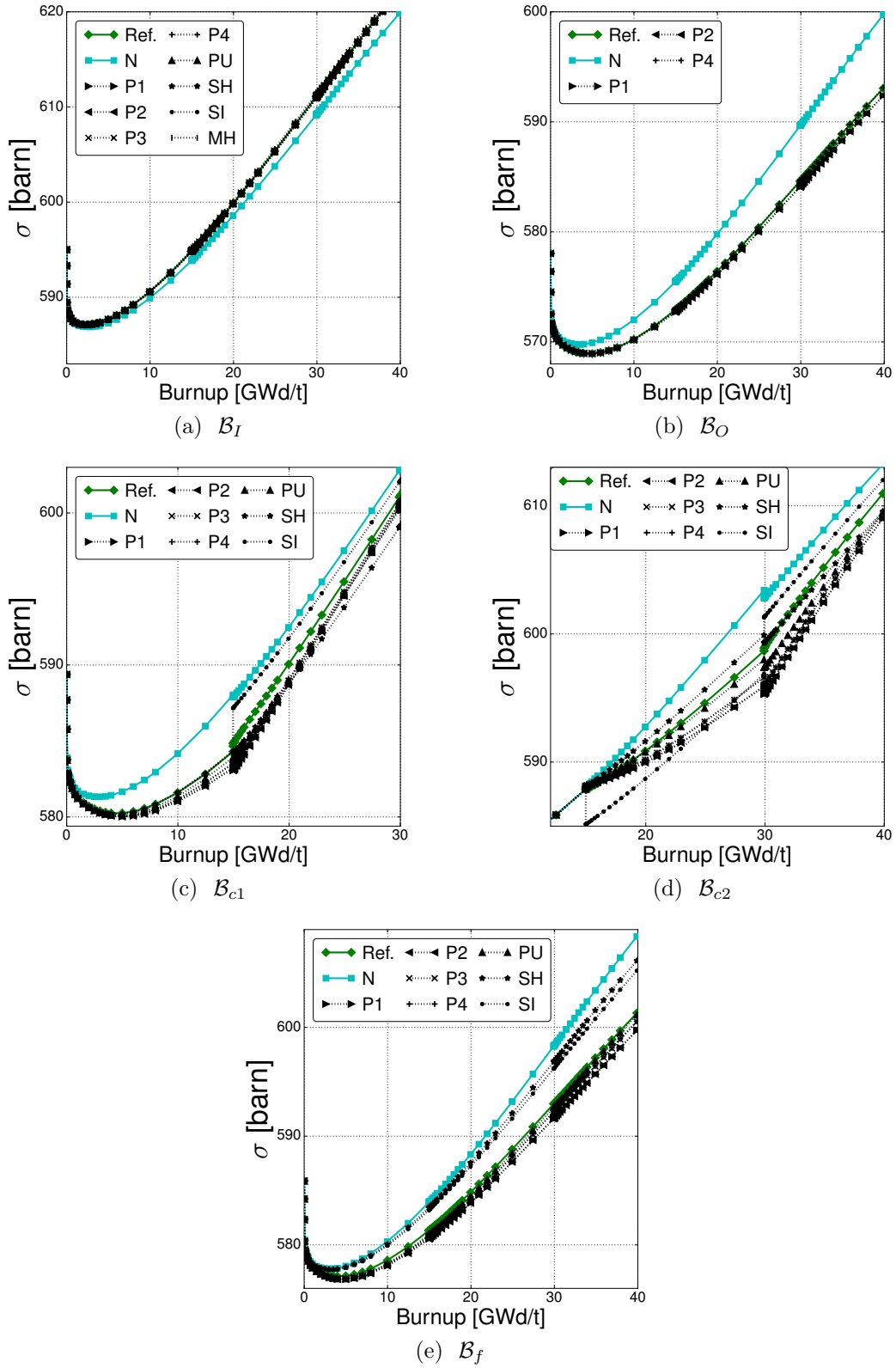


Figure 6: Microscopic cross section  $\nu\sigma_{f,2}$  of  $^{235}\text{U}$  along the burnup with different use cases.

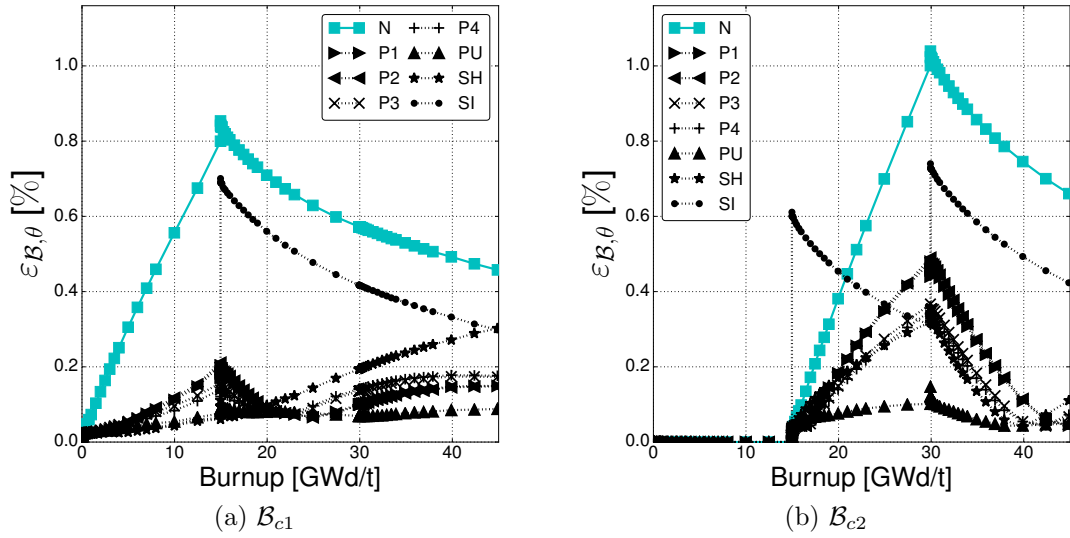


Figure 7: Burnup-dependent average errors of all the microscopic cross sections for all history parameters.

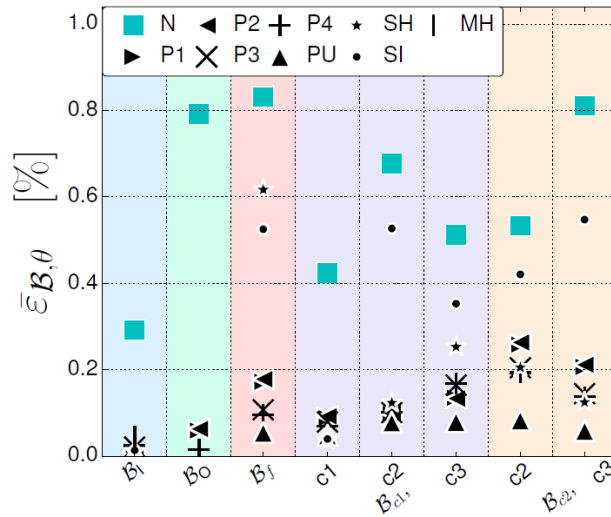


Figure 8: burnup-averaged error with all the history parameters and for the given use cases.

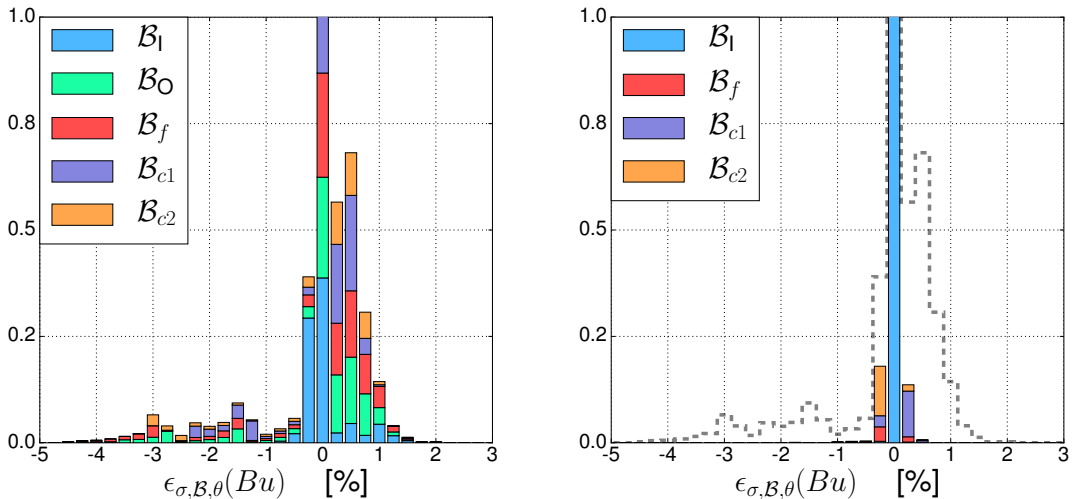
performance is achieved with these cases as expected, since they were used to compute the history coefficients.

For  $\mathcal{B}_f$  a reduction in the error can also be seen, though as noted in literature [24], the spectral methods exhibit poorer performances by reducing the error from 0.8% to about 0.6%. A possible explanation could be in view of the depletion condition, a broadening of the resonances caused by the Doppler effect, that has a direct consequence on the  $^{239}\text{Pu}$  build-up with exposure. As the spectral characteristics of the system are dominated by the moderator, that remains unaltered, spectral-derived history parameter may be inadequate for this case just as it was after the control rod removal, presented in Figure 7a. For example in Figure 2, it can be observed that the parameter P in  $\mathcal{B}_f$  is higher than in  $\mathcal{B}_O$ , whilst the contrary is true for the SI indicating a possible failure of this methodology in reproducing the off-nominal condition. This applied to the SH too, which is derived from the SI.

About  $\mathcal{B}_I$ ,  $\mathcal{B}_O$  and  $\mathcal{B}_f$  the depletion conditions are constant and the cross section error increases linearly with burnup. This means that  $\bar{\varepsilon}_{\mathcal{B},\theta}$  is quite representative of the slope of  $\varepsilon_{\mathcal{B},\theta}(Bu)$ .

As the spectral conditions of the depletion histories are closer to  $\mathcal{B}_O$  than to  $\mathcal{B}_I$ , a marginal gain can indeed be seen with P3 or P4 in comparison to P1 or P2. On the other hand, considering different  $\hat{t}$  (P1 versus P2 or P3 versus P4) does not improve further the error reduction.

Finally Equation 11 is analyzed in view of the standard deviation (SD), the mean and the maximum error of all the cross sections by considering all the reference cases detailed in Section 6. In Figure 9, the error distribution for the microscopic cross sections is presented for  $\sigma_N$  and  $\tilde{\sigma}$  with PU and in Table 4 for all the methods.



(a) Error distribution for  $\sigma_N$ . Peak value of 2.1 (outside chart)

(b) Error distribution for  $\tilde{\sigma}$ , with  $\theta = \text{PU}$ . In dotted line the profile for  $\sigma_N$ . Peak value of 7.4 (outside chart).

Figure 9: Distribution of microscopic cross section error. Bins of 0.25%.

A reduction of 90% in the SD is achieved with the PU method followed by P4, P3 with 83% and then P1 and P2 with 77%. The SH presents a reduction of 47% followed by 34%. A similar trend is found for the maximum error. Uncorrected cross sections do not present any bias, as well as the ones corrected with the history parameters.

Table 4: Standard deviation, mean and maximum error of  $\epsilon_{\sigma,\mathcal{B},\theta}(Bu)$  in %.

|    | MEAN( $\epsilon_{\sigma,\mathcal{B},\theta}(Bu)$ ) | SD     | MAX( $ \epsilon_{\sigma,\mathcal{B},\theta}(Bu) $ ) |
|----|--|--------|---|
| N  | -0.06  | 0.8934 | 4.41  |
| P1 | <0.01  | 0.1984 | 2.98  |
| P2 | <0.01  | 0.2022 | 3.00  |
| P3 | <0.01  | 0.1635 | 2.31  |
| P4 | <0.01  | 0.1389 | 2.27  |
| PU | -0.01  | 0.0878 | 1.79  |
| SH | -0.03  | 0.4688 | 2.96  |
| SI | -0.04  | 0.5755 | 2.40  |
| MH | -0.01  | 0.0653 | 0.45  |

## 7.2 Analysis of the macroscopic cross sections

The input of the nodal equations are macroscopic cross section that define with the flux the reaction rates dictating the state of the core and the fuel evolution. A similar error definition to Equation 11 is here considered:

$$\epsilon_{\Sigma,\mathcal{B},\theta}(Bu) = \tilde{\Sigma}/\Sigma_{\mathcal{B}} - 1. \quad (14)$$

Macroscopic cross sections  $\tilde{\Sigma}$  and  $\Sigma_{\mathcal{B}}$  are computed respectively from  $\tilde{\sigma}$  and  $\sigma_{\mathcal{B}}$  by Equation 2 using the reference concentrations from the case  $\mathcal{B}$  for both of them. Consequently  $\epsilon_{\Sigma,\mathcal{B},\theta}$  relates exclusively to spectrum induced errors, unlike other works where, due to the cross section representation model, nominal concentrations were used for  $\tilde{\Sigma}$ , emphasizing more the history effect [35].

In Figure 10, the burnup-averaged of the relative error in Equation 14:

$$\bar{\epsilon}_{\Sigma,\mathcal{B},\theta} = \frac{1}{\Delta Bu} \int_{Bu_1}^{Bu_2} |\epsilon_{\Sigma,\mathcal{B},\theta}(Bu)| dBu', \quad (15)$$

is presented for  $\mathcal{B}_{c1}$  (with integration per cycle).

A reduction in the error can be seen for every cross section, in particular for the up-scattering  $\Sigma_{2 \rightarrow 1}$ , where the uncorrected error of 1.21% (outside chart) is reduced to about 0.1%. The error of the absorption and of the fission cross section is roughly 0.05%, regardless of the size of the uncorrected error in the thermal group in the first cycle. In the second cycle instead, the history parameterization continues to reduce the error albeit to a lesser extent. As previously explained, the SI can not improve the results after the control rod withdrawal.

In the third cycle of  $\mathcal{B}_{c1}$  and  $\mathcal{B}_f$ ,  $\mathcal{B}_I$  and  $\mathcal{B}_O$  similar reductions in  $\bar{\epsilon}_{\Sigma,\mathcal{B},\theta}$  are observed. They are reported in the Appendix B.

The error  $\bar{\epsilon}_{\Sigma,\mathcal{B},\theta}$  is presented in Figure 11 for the second and for third cycle of  $\mathcal{B}_{c2}$ . Bad results are observed for the fast cross sections  $\Sigma_{a,1}$ ,  $\nu\Sigma_{f,1}$  and  $\Sigma_{1 \rightarrow 2}$ . This is addressed in Section 7.2.1.

The PU methods significantly outperforms the P\* methods especially in these cases, as already noted in Figure 7.1.

The instantaneous behavior of the SI explained for Figure 7 compromises the correction capabilities in both the first and second cycle. Here again a marginal gain can be seen for P3 and P4 in comparison to P1 and P2.

### 7.2.1 Investigation of the poor performances in $\mathcal{B}_{c2}$

The methodologies examined so far could not provide satisfactory corrections with the case  $\mathcal{B}_{c2}$ , which presents the all-rods-in configuration of the assembly all along the second cycle. Varying depletion condi-

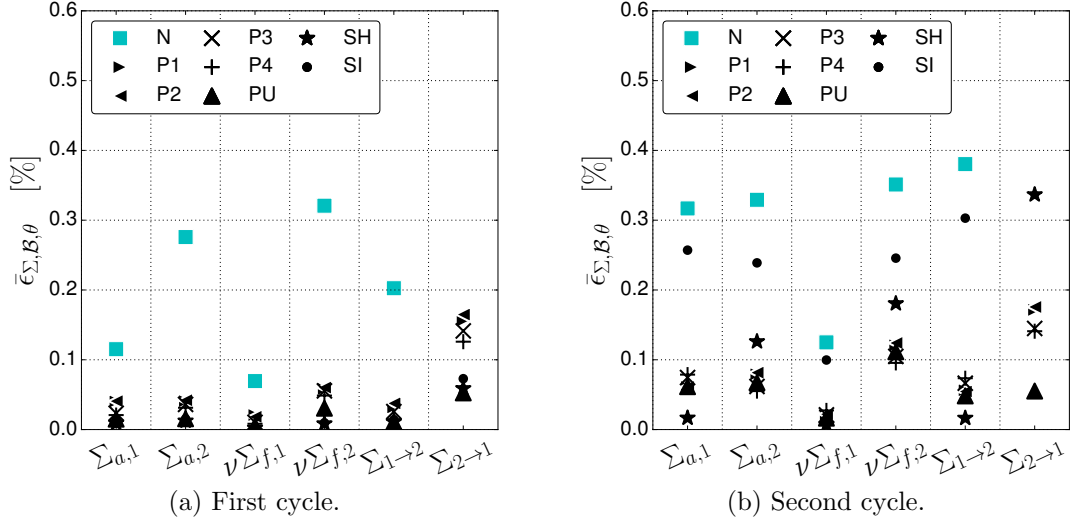


Figure 10:  $\bar{\epsilon}_{\Sigma, \mathcal{B}, \theta}$  error for  $\mathcal{B}_{c1}$ .

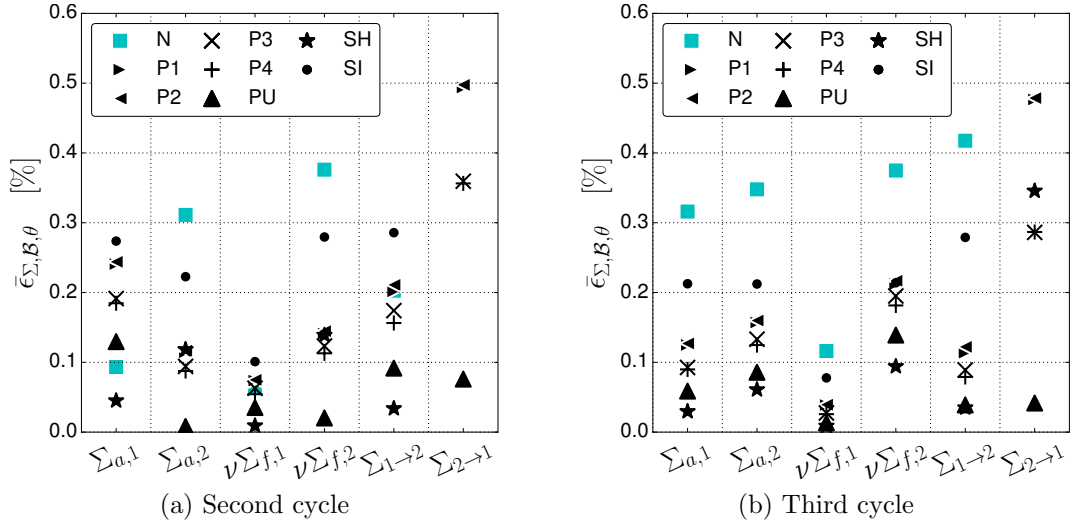


Figure 11:  $\bar{\epsilon}_{\Sigma, \mathcal{B}, \theta}$  error for  $\mathcal{B}_{c2}$ .

tions along the fuel irradiation were noted as very challenging for the modelling of the history effects [35]. In this section, we investigate the causes of the bad performances noticed with the tested parameterizations.

A cumulative error introduced hereafter is used to spot the major contribution to the missed corrections:

$$\epsilon_{j,\Sigma,\mathcal{B},\theta} = \frac{\sum_{i=1}^{I_j} (\sigma_{i,\mathcal{B}} - \tilde{\sigma}_i) C_i}{\Sigma_{\mathcal{B}}}, \quad (16)$$

with the concentration  $C_i$  of the isotope  $i$ ,  $1 \leq i \leq I_j$  and  $1 \leq j \leq I$ .  $I_j$  corresponds to the set of  $j$  isotopes  $\mathcal{I}_j \subseteq \mathcal{I}_I$ , being for instance  $\mathcal{I}_1 = \{^{238}\text{U}\}$ ,  $\mathcal{I}_2 = \{^{238}\text{U}, ^{235}\text{U}\}$ ,  $\dots$ , until finding the full error on the macroscopic cross section  $\Sigma_{\mathcal{B}}$  with  $\mathcal{I}_I$ . This criterion is affected by the compensation of errors with different sign coming from successive isotopes. Hence the  $j$ -th contribution is to be compared with the  $(j-1)$ -th to discriminate the major contributor. The type of cross section with the highest error is the fast neutron absorption, and specifically the one of  $^{240}\text{Pu}$  overshoots the expected correction, see Figure 12. This behavior is observed with all history parameters, as illustrated in Figure 13, where the errors of this cross section averaged within the second cycle are divided by the original errors obtained by the uncorrected  $\sigma_N$ . Values smaller than 1 indicate an improvement with the applied correction, and bad prediction otherwise. Both figures sort the values by isotope according to their importance on the macroscopic cross sections (values indicated in parentheses).

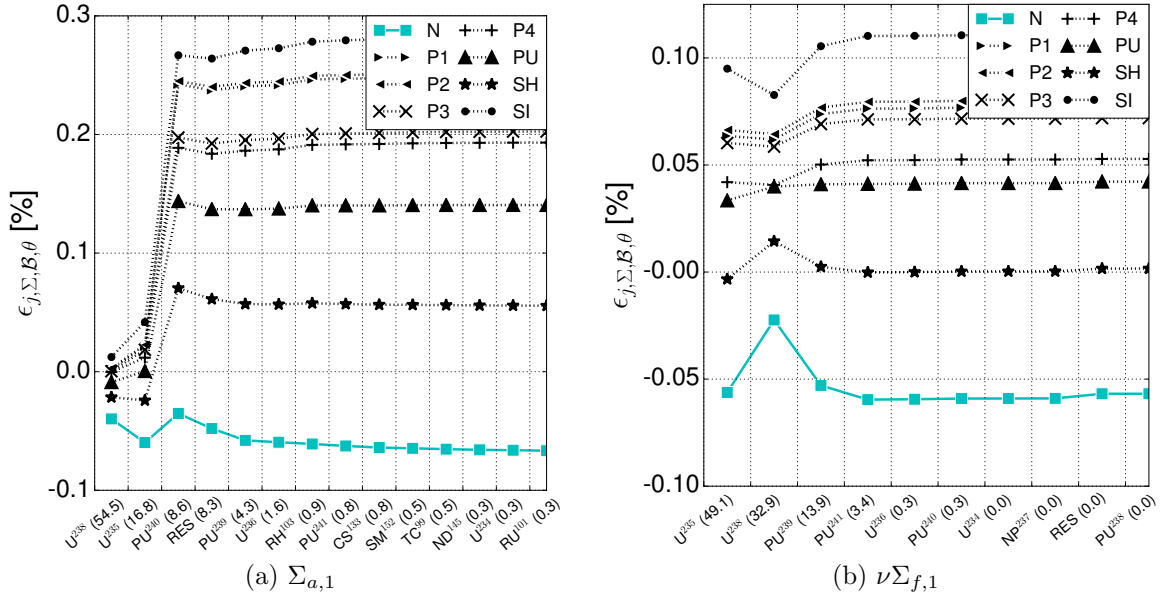


Figure 12: Cumulative error of the macroscopic cross sections in the fast group at 22.5 GWd/t (half of the 2-nd cycle).

About the fission production cross section, the error is mainly determined by  $^{235}\text{U}$ . We also noticed wrong predictions of the up-scattering cross section due to the contribution of the residual mixture, that is  $\Sigma_{2 \rightarrow 1} \approx \Sigma_{2 \rightarrow 1, res}$ . Thermal cross sections were correctly reproduced instead. The methods SH and PU provide the better results. In particular, the slow response in burnup of the SH limits the entity of the unwanted correction.

The control rod insertion in already irradiated fuel induces history effects that become similar to those noticed in  $\mathcal{B}_I$  at the beginning of the cycle, see Figure 14.  $\mathcal{B}_I$  has certainly a more thermal neutron spectrum. The same trend is observed on the concentration and on  $\sigma_{a,1}$  of  $^{240}\text{Pu}$ . The corrections estimated by all methods rely on a supposed spectrum hardening in time, that does not occur at the assumed rate.

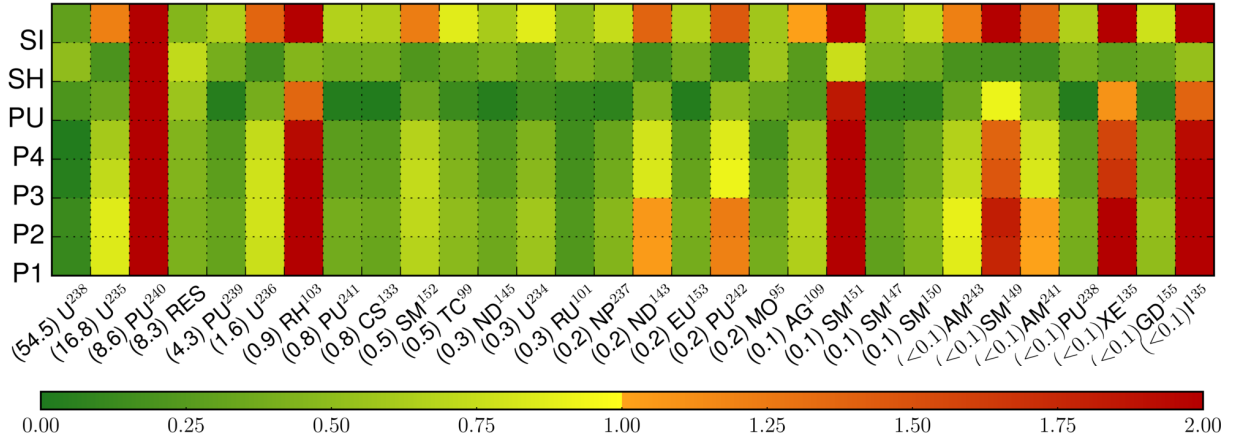
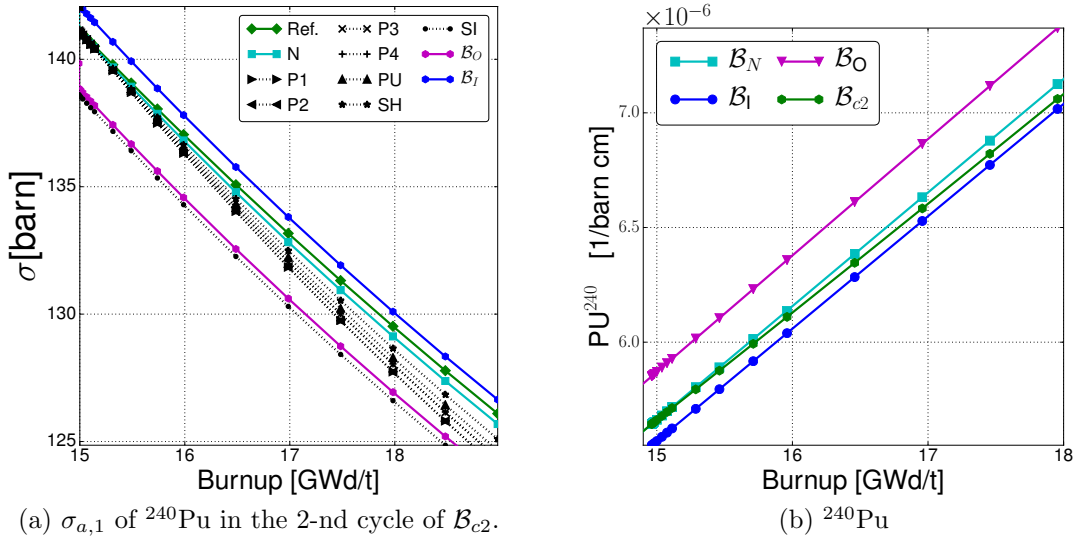


Figure 13: Ratio of the corrected and uncorrected microscopic absorption cross sections in the fast group; the errors are burnup-averaged in the second cycle of  $\mathcal{B}_{c2}$ .

The  $^{240}\text{Pu}$  history coefficient is negative (see Figure 5) and  $\theta_{c2} > \theta_N$  (see Figure 2), thus yielding a correction in the wrong direction for  $\sigma_{a,1}$ .



(a)  $\sigma_{a,1}$  of  $^{240}\text{Pu}$  in the 2-nd cycle of  $\mathcal{B}_{c2}$ .

(b)  $^{240}\text{Pu}$

Figure 14: Concentrations of important isotopes for the reference cases  $\mathcal{B}_{c2}$ ,  $\mathcal{B}_N$ ,  $\mathcal{B}_I$ ,  $\mathcal{B}_O$ .

During the first cycle of  $\mathcal{B}_{c1}$ ,  $^{240}\text{Pu}$  is build-up with a monotone increasing rate by the transmutation of  $^{239}\text{Pu}$  because of the favoured neutron capture under exposure with harder spectrum. In spite of the similar spectral conditions at the beginning of the second cycle in  $\mathcal{B}_{c2}$ , the increasing rate is slowed down by the higher neutron absorpton of  $^{240}\text{Pu}$  with respect to its production. Indeed, the available off-nominal calculations do not show this behavior, suggesting to look for other off-nominal histories at the implementation.

Alternatively, a single history parameter may not be enough to reproduce the history of  $\mathcal{B}_{c2}$ . More independent variables may be necessary for the intended corrections. Also, according to Bilodid [30], a big module of the coefficient, like for  $^{240}\text{Pu}$ , is a marker of high sensitivity of the cross section to the changes

in the concentration of the isotope, and this could demand for the use of non-linear functions.

### 7.3 Analysis of the infinite multiplication factor

The homogenization over the whole fuel assembly quarter yields the macroscopic cross sections describing the multi-group neutron balance equations, which are written as a generalized eigenvalue problem for a two-group infinite homogeneous medium by the introduction of the multiplication factor  $k$ :

$$\begin{cases} (\Sigma_{a,1} + \Sigma_{1 \rightarrow 2}) \phi_1 = \Sigma_{2 \rightarrow 1} \phi_2 + (\nu_1 \Sigma_{f,1} \phi_1 + \nu_2 \Sigma_{f,2} \phi_2) / k, \\ (\Sigma_{a,2} + \Sigma_{2 \rightarrow 1}) \phi_2 = \Sigma_{1 \rightarrow 2} \phi_1. \end{cases} \quad (17)$$

The SI yields straightforwardly the neutron flux in the two-group eigenvalue problem. It is simply determined from the thermal equation as:

$$\text{SI} = (\Sigma_{a,2} + \Sigma_{2 \rightarrow 1}) / \Sigma_{1 \rightarrow 2}. \quad (18)$$

Complementary, the multiplication factor in the infinite medium is:

$$k = \frac{\nu_1 \Sigma_{f,1} \text{SI} + \nu_2 \Sigma_{f,2}}{(\Sigma_{a,1} + \Sigma_{1 \rightarrow 2}) \text{SI} - \Sigma_{2 \rightarrow 1}}. \quad (19)$$

A leakage model can be used to verify the flux conditions used by APOLLO2.8 in burnup calculations, which are depleting the fuel assembly with a critical flux. This is introducing a new term per equation of the kind  $-D_g B^2$  to calibrate the neutron criticality towards  $k = 1$ , being  $D_g$  the diffusion coefficient in the energy group  $g$  and  $B^2$  the material buckling, that acts as an eigenvalue for the new system equations. Hereafter, we examine the performances of the different history models by comparing the eigenpairs of the eigenvalue problems obtained with the corrected cross sections and without any leakage model. The reference values are produced by the cross sections calculated by the lattice code on the curves  $\mathcal{B}$ . The same nuclide concentrations coming from these curves are used to build the macroscopic cross sections with the corrected microscopic cross sections. The relative errors of the two integral parameters are computed as:

$$\epsilon_{\text{SI}, \mathcal{B}, \theta}(Bu) = \tilde{\text{SI}} / \text{SI}_{\mathcal{B}} - 1, \quad (20a)$$

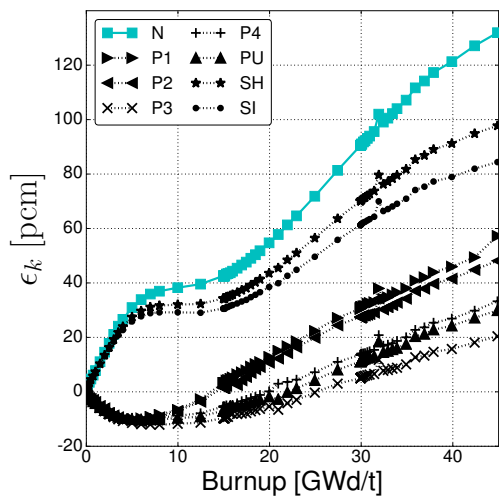
$$\epsilon_{k, \mathcal{B}, \theta}(Bu) = \tilde{k} / k_{\mathcal{B}} - 1. \quad (20b)$$

The Figures 15 plots the evolution of  $\epsilon_k$  in  $\mathcal{B}_f$ ,  $\mathcal{B}_{c1}$  and  $\mathcal{B}_{c2}$ , together with the neutron reactivity along the burnup.

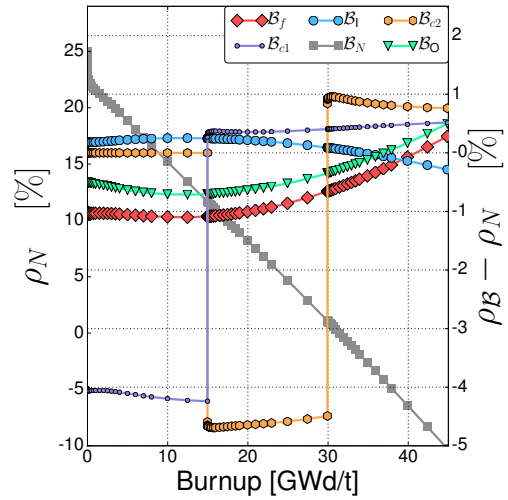
About the cases  $\mathcal{B}_{c1}$  and  $\mathcal{B}_{c2}$ , the corrections achieve a good reduction of  $\epsilon_k$  in the insertion periods. But they can not reproduce correctly the assembly reactivity after the insertion, suggesting a change in the correction methodology at control rod withdrawal by using the SI. The trend observed in  $\mathcal{B}_I$  and  $\mathcal{B}_O$  is very similar to  $\mathcal{B}_f$ . Again, the spectral methods are less effective with the applied corrections.

We remind that the possible improvements observed in the macroscopic cross sections may bring higher error in the fundamental eigen-pair at the end because of systematic error compensation. However, the differences in the original uncorrected reactivities are rather small compared to those arising in the core calculations, due to the uncertainty related to the physical core state and to the nuclide concentrations.

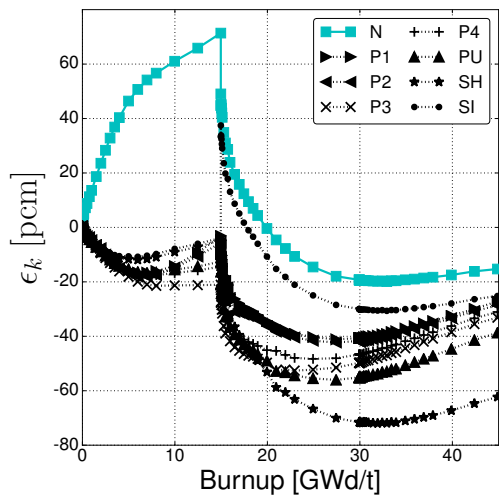
The standard deviation, the mean and the maximum absolute error of  $\epsilon_k$  are presented in Table 5 for all the history parameters. The statistics take into account the values from all the available cases from Section 6. The Pu methods manage on average to get better results. The method MH is only tested against  $\mathcal{B}_I$ , for lack of cases with a different moderator density during depletion; at least in this test case, it performs reasonably well. The distribution of these errors are also shown in the Figures 16, where only the method PU is reported, being the most successful. The components from the separate cases appear with different colors in the columns of the histograms.



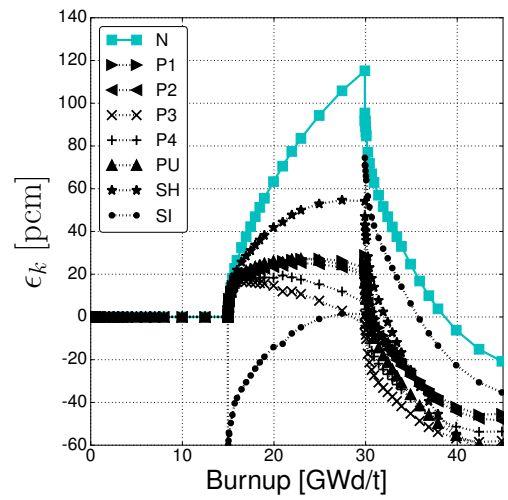
(a)  $\mathcal{B}_f$



(b)  $\rho_N$  shown in the left axis and  $\rho_B - \rho_N$  to the right.

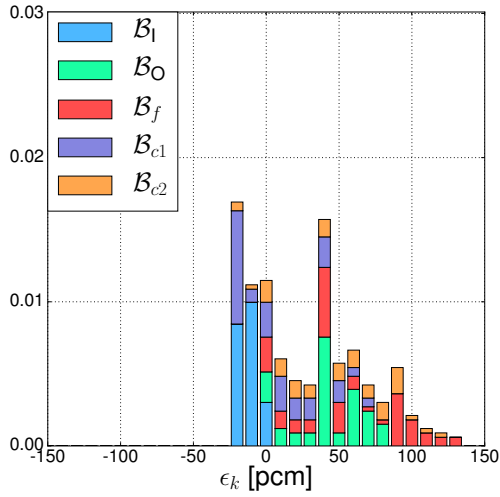


(c)  $\mathcal{B}_{c1}$

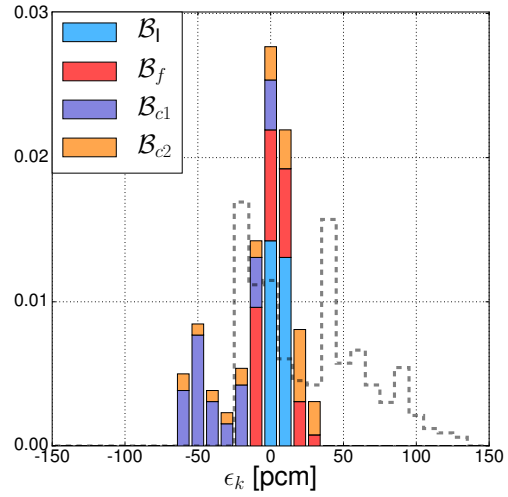


(d)  $\mathcal{B}_{c2}$

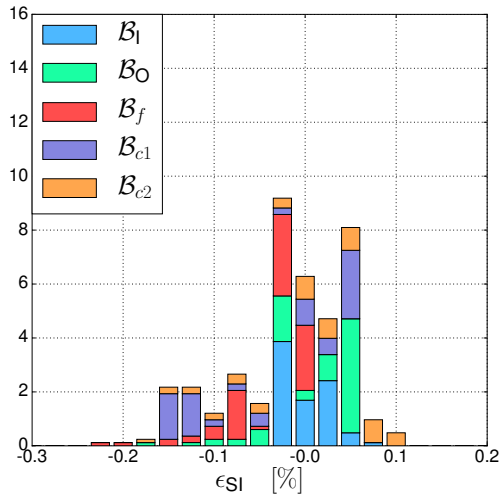
Figure 15:  $\epsilon_k$  with the different correction methods, with the neutron reactivity of all use cases (top left).



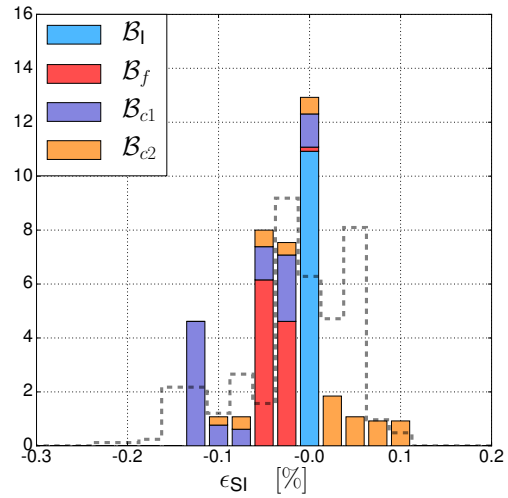
(a) Without correction



(b) PU



(c) Without correction



(d) PU

Figure 16: Histograms of  $\epsilon_k$  and  $\epsilon_{SI}$  (uncorrected profile in dotted line); bins of 10 pcm and 0.025% respectively.

Table 5: Standard deviation (SD), mean and maximum absolute error (MAX) of  $\epsilon_k$  in pcm and of  $\epsilon_{SI}$  in %.

|    | $\epsilon_k$ |    |     | $\epsilon_{SI}$ |       |       |
|----|--------------|----|-----|-----------------|-------|-------|
|    | MEAN         | SD | MAX | MEAN            | SD    | MAX   |
| N  | 27           | 39 | 132 | -0.017          | 0.062 | 0.217 |
| P1 | 2            | 20 | 57  | -0.014          | 0.048 | 0.138 |
| P2 | -0           | 20 | 48  | -0.010          | 0.048 | 0.151 |
| P3 | -10          | 21 | 59  | -0.027          | 0.052 | 0.129 |
| P4 | -5           | 19 | 54  | -0.028          | 0.049 | 0.134 |
| PU | -7           | 23 | 61  | -0.028          | 0.048 | 0.134 |
| SH | 6            | 40 | 98  | -0.025          | 0.050 | 0.153 |
| SI | 10           | 31 | 84  | -0.026          | 0.053 | 0.141 |
| MH | 8            | 6  | 20  | 0.002           | 0.001 | 0.006 |

The reduction in the standard deviation is strongly driven by the reference cases  $\mathcal{B}_I$  and  $\mathcal{B}_f$ . The missed corrections after the rods withdrawal in  $\mathcal{B}_{c1}$  and  $\mathcal{B}_{c2}$  are the main cause for the high tail in Figure 7.3, with errors of about -50 pcm in  $\tilde{k}$ .

## 8 Conclusion

This work discussed a few relevant history effects in PWR analysis caused by the approximations of the standard cross section preparation. These effects arise in core calculations whenever the fuel assemblies are burning for prolonged periods in time at different exposure conditions other than the ones used by the lattice code in burnup calculations. In fact, the traditional cross section preparation is generally reproducing the behavior of the fuel at normal operation on base power load, allowing only short variations in time of the core state. Recent design of PWR units and boron-free SMRs largely employs protracted mechanical shim to control and operate the reactor, thus incurring in possible issues with the modelling of the history effects.

Indeed, this constitutes a well-known problem since the beginning of the development of light water reactor technology, thus motivating the literature review which is at the base of this article. This review suggests possible resolutions by increasing the number of specialized isotopes in the reduced depletion chains, and the introduction of various models to correct the homogenized cross sections directly online during the core calculation. These methodologies are here reviewed and tested with a set of depletion histories of topical interest on a typical UO<sub>2</sub> 17 × 17 fuel assembly, whose data specifications follow from the “Burn-up Credit Criticality Benchmark: Phase II-D”.

Although some methods came originally with empirical formulae, we propose here a common expression justified by a first order Taylor expansion which offer also a common background for their implementation and discussion. A comparison of the Taylor coefficients for the first derivative approximated at the core inlet and outlet seems indicating possible non-linear behaviors, likely recoverable by higher order terms in the expansion. On the other hand, a weak dependence on the instantaneous parameters of the history coefficients is noted, thence allowing to avoid additional branch calculations on the off-nominal burnup calculations. This interesting outcome limits the implementation effort in the existing schemes of cross section preparation based on lookup tables.

We used a representative list of isotopes in our reduced depletion chain to cover the majority of core applications with the current standards in industry. The list is fine enough to yield small errors in the

neutron reactivity and in the spectral index of the fundamental flux calculated with the two group cross sections, which are spatially homogenized in the fuel assembly quarter. The reference nuclide concentrations were used in all tests in order to restrain the source of error to the only microscopic cross sections. Furthermore, all cross sections requested at the given instantaneous state parameters were produced by lattice calculations, without making any approximation by the common data interpolation. The errors noticed in our tests must then be considered as a lower bound for the real error in core calculations, due to the additional differences arising in the nuclide inventory along exposure.

About the microscopic cross sections, a general reduction of the error is observed with all the history parameters, but in the use case  $\mathcal{B}_{c2}$ . In this case all methods failed with the fast absorption cross section of  $^{240}\text{Pu}$ . This outcome is not noticed in  $\mathcal{B}_{c1}$  suggesting that a dedicated off-nominal calculation should be used to reproduce the physics of plutonium during protracted insertion periods in spent fuel with relevant amount of  $^{240}\text{Pu}$ .

About the history parameterization, the Pu methods performed better than the spectral methods, with the PU method showing the best results in all test cases. In particular, the spectral methods did not provide any benefit with the case  $\mathcal{B}_f$ . The SH avoids however the sudden changes in value characterizing the SI and canceling the potential corrections. In conclusion our recommendation is to use the parameter PU.

Our study considers only standard uranium fuel. This analysis should be continued with other fuel types to provide general recommendations for core calculations.

## Acknowledgement

The authors are grateful to Antonio Galia for his extensive support with the APOLLO2.8 calculations.

## References

- [1] Barreau A. Burn-up Credit Criticality Benchmark. OECD-NEA; 2006. Phase, IID and Assembly, PWRUO. PWR-UO2 Assembly Study of Control Rod Effects on Spent Fuel Composition.
- [2] Lawrence R. Progress in nodal methods for the solution of the neutron diffusion and transport equations. *Progress in Nuclear Energy*. 1986;17(3):271–301.
- [3] Smith KS. Assembly homogenization techniques for light water reactor analysis. *Progress in Nuclear Energy*. 1986;17(3):303–335.
- [4] Hebert A. A consistent technique for the pin-by-pin homogenization of a pressurized water reactor assembly. *Nuclear Science and Engineering*. 1993;113(3):227–238.
- [5] Sanchez R. Assembly homogenization techniques for core calculations. *Progress in Nuclear Energy*. 2009;51(1):14–31.
- [6] Martin N, Riedmann M, Bigot J. Latest developments in the artemis tm core simulator for bwr steady-state and transient methodologies. Jeju, Korea. AREVA; 2017. International Conference on Mathematics and Computational Methods Applied to Nuclear Science and Engineering.
- [7] Stamm'ler R, Abbate M. *Methods of steady-state reactor physics in nuclear design*. Academic Press; 1983.
- [8] Müller E, Mayhue L, Zhang B. Reactor physics methods development at Westinghouse. In: *Proc. Int. Conf. Nuclear Energy for New Europe 2007*; 2007.
- [9] Hino T, et al. Core design and analysis of axially heterogeneous boiling water reactor for burning transuranium elements. *Nuclear Science and Engineering*. 2017;187:3:213–239.
- [10] Grossetete A. Le pilotage de l'EPR: mode T. *Revue générale nucléaire*. 2007;(3):37–41. (in French).
- [11] Onoue M, Kawanishi T, Carlson WR, et al. Application of MSHIM core control strategy for Westinghouse AP1000 nuclear power plant. *GENES4/ANP2003*. 2003;:15–18.
- [12] van der Merwe L, Hah CJ. Reactivity balance for a soluble boron-free small modular reactor. *Nuclear Engineering and Technology*. 2018; Available from: <http://www.sciencedirect.com/science/article/pii/S1738573317308161>.
- [13] Choe J, Shin HC, Lee D. Optimal Control Rod for Boron-Free Small Modular PWR. In: *Proceedings of The 20th Pacific Basin Nuclear Conference*; Singapore. Springer Singapore; 2017. p. 809–815.
- [14] Kim H, Chung C, Yahya M, et al. Core reactivity control for a soluble boron free small modular reactor. *American Nuclear Society*. 2017;116.
- [15] Tomatis D, Galia A, Pastoris S, et al. Quantification of history effects in pwr modelling. *Nuclear Engineering and Design*. 2017;325:205 – 217.
- [16] Dall'Osso A. Modeling local history effects in the nodal core ARTEMIS. *International Conference on Mathematics and Computational Methods Applied to Nuclear Science and Engineering*. 2017;.
- [17] Mosteller R. Impact of moderator history on physics parameters in pressurized water reactors. *Nuclear Science and Engineering*. 1988;98(2):149–153.
- [18] Guimarães P, Müller E. Parameterization of two-group nodal cross section data for POLCA-T BWR transient applications. In: *International Conference on Mathematics, Computational Methods, & Reactor Physics*; 2009.
- [19] Bahadir T, Lindahl S, Palmtag S. Simulate-4 multigroup nodal code with microscopic depletion model. *Mathematics and Computation, Supercomputing, Reactor Physics and Nuclear and Biological Applications*. 2005;.

- [20] Fujita T, Endo T, Yamamoto A. A macroscopic cross-section model for bwr pin-by-pin core analysis. *Journal of Nuclear Science and Technology*. 2014;51(3):282–304. Available from: <https://doi.org/10.1080/00223131.2014.864248>.
- [21] Rempe KR, Smith KS, Henry AF. Simulate-3 pin power reconstruction: Methodology and benchmarking. *Nuclear Science and Engineering*. 1989;103:334–342.
- [22] Lee C, Kim Y, Song J, et al. Incorporation of a new spectral history correction method into local power reconstruction for nodal methods. *Nuclear science and engineering*. 1996;124(1):160–166.
- [23] Iwamoto T, Yamamoto M. Advanced nodal methods of the few-group BWR core simulator NEREUS. *Journal of nuclear science and technology*. 1999;36(11):996–1008.
- [24] Baturin D, Vygovskii S. Taking account of the spectral history of fuel burnup during the preparation of the neutron-physical constants for VVER-1000 fuel assemblies. *Atomic Energy*. 2001;90(4):267–272.
- [25] Aragonés JM. Fundamentals of 3-D Neutron Kinetics and Current Status [Thicbaocheng zhang, toshikazu ida, [6] ket-2008, csni-nea-ocde seminar, pisa (italy)]; 2008.
- [26] Ida T, Tahara Y. Two group micro-depletion correction model for ALPHA/PHOENIX-P/ANC code system ; 2000.
- [27] Zhang B, Ida T, Barreau A, et al. A study on generic two-group cross-section representation methodology ; 2002.
- [28] Mayhue, Larry, Zhang, et al. Pwr core modeling using the nexus once-through cross-section model ; 2006.
- [29] Bilodid I, Mittag S. Use of the local Pu-239 concentration as an indicator of burnup spectral history in DYN3D. *Annals of Nuclear Energy*. 2010;37(9):1208–1213.
- [30] Bilodid Y. Spectral History Modeling in the Reactor Dynamics Code DYN3D. *Technischen Universitat Dresden*. 2014;.
- [31] Bilodid Y, Fridman E, Kliem S. Microscopic depletion with the correction of microscopic cross section nodeal diffusion code dyn3d. *PHYSOR*. 2016;.
- [32] Girieud. SCIENCE, Version 2: The Most Recent Capabilities of the Framatome 3D Nuclear Code Package. *FRAMATOME Nuclear Operations*. 2000;.
- [33] Sarwar R. Validation of POLCA7 Cross section Model. *Chalmers university of technology*. 2013;.
- [34] Rosman K, Taylor P. Isotopic composition of the elements 1997. *Pure and Applied Chemistry*. 1998; 70(1):217–235.
- [35] Li Y, Gao S, Wu H, et al. PWR few-group constants parameterization analysis. *Progress in Nuclear Energy*. 2016;88:204–117.
- [36] at al RS. APOLLO2 Year 2010. *Nucl Eng and Technology*. 2010;42:474–499.
- [37] Hébert A. *Applied reactor physics*. Presses inter Polytechnique; 2009.
- [38] Coste-Delclaux M. Modélisation du phénomène d'autoprotection dans le code de transport multi-groupe APOLLO2. *CEA-R-6114*. 2006;(in French).

## A APOLLO2.8 calculations

The lattice calculations were performed using the code APOLLO2.8 [36] with a 281-group cross section library based on JEFF-3.1.1, with the flux solver based on the method of characteristics (MOC) and the  $P_3$  anisotropic scattering. The  $B_1$  fundamental mode leakage model was imposed to obtain a critical flux [37].

The calculation uses the predictor-corrector scheme based on polynomial interpolation of the reaction rates, while solving the Bateman equations with the fourth order Runge-Kutta method. At each depletion step the flux is recalculated with new self-shielded cross-sections. The standard self-shielding options of APOLLO2.8, based on Livolant-Jeanpierre formalism are used [38, 37]. The ordinary fuel pin is spatially divided in four annular regions in the self-shielding calculations. Self-shielding is done for all actinide isotopes, principal fission products and the constituents of the cladding, burnable absorber pins and control rods. These are:  $^{107}\text{Ag}$ ,  $^{109}\text{Ag}$ ,  $^{110}\text{Cd}$ ,  $^{113}\text{Cd}$ ,  $^{241}\text{Am}$ ,  $^{243}\text{Am}$ ,  $^{nat}\text{Cr}$ ,  $^{133}\text{Cs}$ ,  $^{153}\text{Eu}$ ,  $^{nat}\text{Fe}$ ,  $^{154}\text{Gd}$ ,  $^{155}\text{Gd}$ ,  $^{156}\text{Gd}$ ,  $^{157}\text{Gd}$ ,  $^{158}\text{Gd}$ ,  $^{160}\text{Gd}$ ,  $^{115}\text{In}$ ,  $^{95}\text{Mo}$ ,  $^{143}\text{Nd}$ ,  $^{145}\text{Nd}$ ,  $^{nat}\text{Ni}$ ,  $^{237}\text{Np}$ ,  $^{238}\text{Pu}$ ,  $^{239}\text{Pu}$ ,  $^{240}\text{Pu}$ ,  $^{241}\text{Pu}$ ,  $^{242}\text{Pu}$ ,  $^{103}\text{Rh}$ ,  $^{101}\text{Ru}$ ,  $^{147}\text{Sm}$ ,  $^{149}\text{Sm}$ ,  $^{150}\text{Sm}$ ,  $^{151}\text{Sm}$ ,  $^{152}\text{Sm}$ ,  $^{99}\text{Tc}$ ,  $^{234}\text{U}$ ,  $^{235}\text{U}$ ,  $^{236}\text{U}$ ,  $^{238}\text{U}$  and  $^{nat}\text{Zr}$ . The options for the treatment of the resonance interferences (resonant mixtures model) are chosen for  $^{235}\text{U}$ ,  $^{238}\text{U}$ ,  $^{239}\text{Pu}$  and  $^{240}\text{Pu}$ .

The spatial mesh used in the MOC flux calculation is presented in Fig. 17. Every ring depletes independently in every pin. While the sets of four self-shielded cross sections are shared between five groups of pins, which are classified according to the similarities in their positional surroundings.

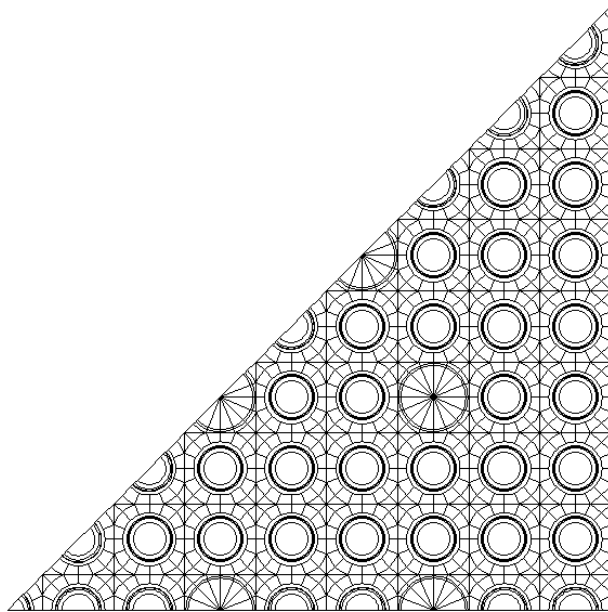


Figure 17: Spatial mesh of the MOC solver used to calculate one eighth of the  $17 \times 17$  cell symmetric assembly.

## B Macroscopic cross sections error

In Table 6-9 macroscopic cross section errors are presented for the different history parameters. A major improvement in the macroscopic cross section error can be seen for both  $\mathcal{B}_I$  and  $\mathcal{B}_O$ .

Table 6:  $\bar{\epsilon}_\Sigma$  average in the third cycle (from 30 GWd/tU to 45 GWd/tU) for the case  $\mathcal{B}_{c1}$ .

|    | $\bar{\epsilon}_{\Sigma, \mathcal{B}, \theta}$ |                |                   |                   |                                |                                |
|----|--|----------------|-------------------|-------------------|--------------------------------|--------------------------------|
|    | $\Sigma_{a,1}$                                 | $\Sigma_{a,2}$ | $\nu\Sigma_{f,1}$ | $\nu\Sigma_{f,2}$ | $\Sigma_{g_1 \rightarrow g_2}$ | $\Sigma_{g_2 \rightarrow g_1}$ |
| N  | 0.27   | 0.19           | 0.09              | 0.19              | 0.32                           | 1.26                           |
| P2 | 0.10   | 0.01           | 0.04              | 0.03              | 0.12                           | 0.24                           |
| P1 | 0.11   | 0.01           | 0.04              | 0.03              | 0.12                           | 0.24                           |
| P4 | 0.13   | 0.02           | 0.04              | 0.02              | 0.14                           | 0.32                           |
| P3 | 0.13   | 0.01           | 0.04              | 0.02              | 0.13                           | 0.32                           |
| PU | 0.09   | 0.03           | 0.03              | 0.08              | 0.09                           | 0.08                           |
| SH | 0.03   | 0.19           | 0.02              | 0.27              | 0.08                           | 0.77                           |
| SI | 0.20   | 0.11           | 0.07              | 0.10              | 0.23                           | 0.83                           |

Table 7:  $\bar{\epsilon}_\Sigma$  average in the three cycles for  $\mathcal{B}_I$ .

|    | $\bar{\epsilon}_{\Sigma, \mathcal{B}, \theta}$ |                |                   |                   |                                  |                                  |
|----|--|----------------|-------------------|-------------------|----------------------------------|----------------------------------|
|    | $\Sigma_{a,1}$                                 | $\Sigma_{a,2}$ | $\nu\Sigma_{f,1}$ | $\nu\Sigma_{f,2}$ | $\Sigma_s^{g_1 \rightarrow g_2}$ | $\Sigma_s^{g_2 \rightarrow g_1}$ |
| N  | 0.12   | 0.16           | 0.04              | 0.18              | 0.15                             | 0.79                             |
| P1 | <0.01  | 0.00           | <0.01             | <0.01             | <0.01                            | <0.01                            |
| P2 | <0.01  | <0.01          | <0.01             | <0.01             | <0.01                            | <0.01                            |
| P3 | 0.02   | 0.01           | <0.01             | 0.01              | 0.01                             | 0.05                             |
| P4 | 0.02   | 0.01           | 0.01              | 0.01              | 0.02                             | 0.05                             |
| PU | 0.01   | 0.0            | <0.01             | <0.01             | 0.01                             | 0.02                             |
| SH | 0.01   | 0.0            | <0.01             | <0.01             | 0.01                             | 0.03                             |
| SI | 0.02   | 0.01           | 0.01              | <0.01             | 0.01                             | 0.03                             |
| MH | <0.01  | 0.02           | <0.01             | 0.03              | 0.01                             | 0.12                             |

Table 8:  $\bar{\epsilon}_\Sigma$  average in the three cycles for  $\mathcal{B}_O$ .

|    | $\bar{\epsilon}_{\Sigma, \mathcal{B}, \theta}$ |                |                   |                   |                                |                                |
|----|--|----------------|-------------------|-------------------|--------------------------------|--------------------------------|
|    | $\Sigma_{a,1}$                                 | $\Sigma_{a,2}$ | $\nu\Sigma_{f,1}$ | $\nu\Sigma_{f,2}$ | $\Sigma_{g_1 \rightarrow g_2}$ | $\Sigma_{g_2 \rightarrow g_1}$ |
| N  | 0.3  | 0.45           | 0.12              | 0.52              | 0.41                           | 2.1                            |
| P1 | 0.05   | 0.02           | 0.01              | 0.01              | 0.03                           | 0.14                           |
| P4 | 0.01   | 0.01           | 0.01              | 0.01              | 0.02                           | 0.01                           |
| P3 | 0.00   | 0.00           | 0.00              | 0.00              | 0.00                           | 0.00                           |
| P2 | 0.05   | 0.02           | 0.02              | 0.02              | 0.04                           | 0.15                           |
| PU | 0.00   | <0.01          | <0.01             | <0.01             | <0.01                          | <0.01                          |
| SH | <0.01  | <0.01          | <0.01             | <0.01             | <0.01                          | <0.01                          |
| SI | <0.01  | <0.01          | <0.01             | <0.01             | <0.01                          | <0.01                          |
| MH | <0.01  | <0.01          | <0.01             | <0.01             | <0.01                          | <0.01                          |

Table 9:  $\bar{\epsilon}_\Sigma$  average in the three cycles for  $\mathcal{B}_f$ .

|    | $\bar{\epsilon}_{\Sigma, \mathcal{B}, \theta}$ |                |                   |                   |                                |                                |
|----|--|----------------|-------------------|-------------------|--------------------------------|--------------------------------|
|    | $\Sigma_{a,1}$                                 | $\Sigma_{a,2}$ | $\nu\Sigma_{f,1}$ | $\nu\Sigma_{f,2}$ | $\Sigma_{g_1 \rightarrow g_2}$ | $\Sigma_{g_2 \rightarrow g_1}$ |
| N  | 0.27   | 0.46           | 0.14              | 0.52              | 0.46                           | 2.21                           |
| P2 | 0.14   | 0.09           | 0.03              | 0.12              | 0.07                           | 0.42                           |
| P1 | 0.14   | 0.08           | 0.03              | 0.11              | 0.06                           | 0.42                           |
| P4 | 0.07   | 0.05           | 0.01              | 0.08              | 0.01                           | 0.24                           |
| P3 | 0.08   | 0.06           | 0.01              | 0.09              | 0.02                           | 0.25                           |
| PU | 0.06   | 0.03           | 0.01              | 0.05              | 0.02                           | 0.08                           |
| SH | 0.19   | 0.34           | 0.10              | 0.38              | 0.35                           | 1.64                           |
| SI | 0.15   | 0.29           | 0.09              | 0.32              | 0.30                           | 1.40                           |